Cast shadows reveal changes in glacier ~~thickness~~surface elevation

Monika Pfau[1], Georg Veh[1], Wolfgang Schwanghart[1]

[1]Department of Environmental Sciences and Geography, University of Potsdam, Potsdam, 14476, Germany

Correspondence to: Monika Pfau (monika.pfau@arcor.de)

Abstract. Increased rates of glacier retreat and thinning call for accurate local estimates of glacier elevation change to predict future changes in glacier runoff and their contribution to sea level rise. Glacier elevation change is typically derived from digital elevation models (DEMs) tied to surface change analysis from satellite imagery. Yet, the rugged topography in mountain regions can cast shadows onto glacier surfaces, making it difficult to detect local glacier elevation changes in remote areas. ~~However, most optical satellite images offer~~ A rather untapped resource are precise, time-stamped data on ~~precise time-stamped meta data of the~~ solar position and angle in satellite images~~during the acquisition~~. These data are useful to simulate shadows from a given DEM. Accordingly, any differences in shadow length between simulated and mapped shadows in satellite images could indicate a change in glacier elevation relative to the acquisition date of the DEM. We tested this hypothesis at five selected glaciers with long-term monitoring programs. For each glacier, we projected cast shadows on the glacier surface from freely available DEMs and compared simulated shadows to cast shadows mapped ~~in~~ from ~40 years of Landsat images. We validated the relative differences with *in situ* geodetic measurements of glacier elevation change where these shadows occurred. We find that shadow-derived glacier elevation changes are consistent with independent photogrammetric and geodetic surveys in shad~~ow~~ed areas. ~~Our method shows that~~Accordingly, a shadow cast on Baltoro Glacier (Karakoram, Pakistan) ~~gained~~ suggests ~~slightly local increases~~no changes in elevation between 1987 and 2020, while shadows on Great Aletsch Glacier (Switzerland) ~~recorded~~ point to the most negative thinning rates of about 1 m per year in our sample. Our estimates of glacier elevation change are tied to occurrence of mountain shadows, and may help complement field campaigns in regions that are difficult to access. ~~Our approach provides local glacier thickness changes, a vital~~ This information can be vital to quantify possibly varying elevation-dependent changes in the accumulation or ablation zone of a given glacier. Shadow-based retrieval of glacier elevation changes hinges on the precision of the DEM as the geometry of ridges and peaks constrain the shadow that we cast on the glacier surface. Future generations of DEMs with higher resolution and accuracy will improve our method, enriching the toolbox for tracking historical glacier mass balances from satellite and aerial images~~ especially in remote glacier areas with difficult field access~~.

1 Introduction

Quantifying spatial and temporal patterns of glacial changes is important to understand the response of the cryosphere to ongoing atmospheric warming (IPCC 2019). Changes in glacier volume determine the availability of regional and local freshwater resources that support the basic needs of many millions of people living in glaciated river basins (IPCC 2019; Pritchard 2019; Azam et al. 2021). Glacier retreat can shift ecosystems higher in elevation, changing the composition of, and possibly creating new, habitats (Brighenti et al. 2019; Cauvy-Fraunié and Dangles 2019). Shrinking glaciers also alter discharge seasonality, enhance rates of sediment transport, and shift biogeochemical and contaminant fluxes in glaciated river basins (Milner et al. 2017; Li et al. 2021~~; Milner et al. 2017~~). In high mountains, glacier retreat can also destabilize adjacent hillslopes, possibly enhancing the frequency and magnitude of catastrophic slope failures (Huggel et al. 2012). Other hazards to mountain communities evolve from new meltwater lakes that can suddenly empty in glacial lake outburst floods (Veh et al. 2020). Recent appraisals entail that ice loss has accelerated globally in past decades, with thinning rates of glaciers outside the Antarctic and Greenland ice sheets having doubled between 2000 and 2019 (Hugonnet et al. 2021). Still, some 141,000 km³ of glacier ice cover ~10% of the Earth's land surface today (Farinotti et al. 2019; Millan et al. 2022). Given projected future warming scenarios, sustainable management of these remaining ice resources requires accurate knowledge of regional and local mass balances (Richardson and Reynolds 2000; Bolch et al. 2011).

Measuring changes in the surface elevation of glaciers relies on repeated field and remote-~~-~~sensing based surveys. Space-borne techniques such as laser altimetry (e.g., ICESat) (Moholdt et al. 2010; Neckel et al. 2014), radar interferometry (Farías-Barahona et al. 2020) or stereo-photogrammetry (Bolch et al. 2011) helped quantify changes in glacier surface elevation over large spatial scales and in terrain which is difficult to access. These appraisals are largely constrained to the past two decades, with few exceptions such as Corona and Hexagon missions (Belart et al. 2020; Geyman et al. 2022; Mannerfelt et al. 2022), which provided one-time stereo image pairs between the 1960s and 1970s (Lovell et al. 2018; Dehecq et al. 2020). Other space-borne derived estimates of long-term glacier changes have relied on time series of optical satellite images, yet without the capability of using stereo-photogrammetry. The Landsat mission has been particularly useful for mapping changes in glacier area, rather than elevation, primarily due to continuous recording period extending back to the 1970s, the high temporal repetition rate of 16 days, and a moderate spatial resolution of 30 m in the visible to shortwave infrared electromagnetic spectrum (Paul et al. 2011; Wulder et al. 2019; Wulder et al. 2022). If intersected with a DEM, glacier outlines mapped from~~in~~ Landsat (or any other satellite or aerial) images can ~~help reveal~~be used to estimate changes in glacier elevation (Rankl and Braun 2016; Zhang et al. 2016~~; Rankl and Braun 2016~~).

While optical satellite and aerial imagery provides the longest, remotely sensed records of glacier change, its analysis is challenging in topographic settings where high relief casts shadows on highly reflective glacier surfaces (Kääb et al. 2016). As mountains block the direct incoming solar radiation, shad~~ow~~ed glacier surfaces are characterized by a low variation of radiometric values, thus complicating visual image interpretation or automated approaches of image classification (Richter

1998; Paul et al. 2002; Racoviteanu and Williams 2012; Li et al. 2016). The problem of cast shadows increases with latitude owing to seasonal differences in solar elevation angle, and with the height of mountains, as those can cast wider shadows. Against these known limitations, we hypothesize that cast shadows in optical satellite images also have a largely untapped potential for mapping glacier elevation changes. If the local glacier elevation has changed in two successive time steps, the shape of shadows emanating from adjacent mountains has to change accordingly, as long as solar elevation, azimuth, and the geometry of ridges and peaks remain constant (Fig. 1). Therefore, we expect that glacier thinning must locally cause longer shadows, while a local gain in glacier thickness will shorten the length of shadows. Using the tangent, the horizontal offset can be converted into a vertical displacement, i.e. a change in elevation. These changes in elevation can also be translated into estimates of glacier altitude using a ~~digital elevation model (~~DEM~~)~~ as a reference (Fig. 1).

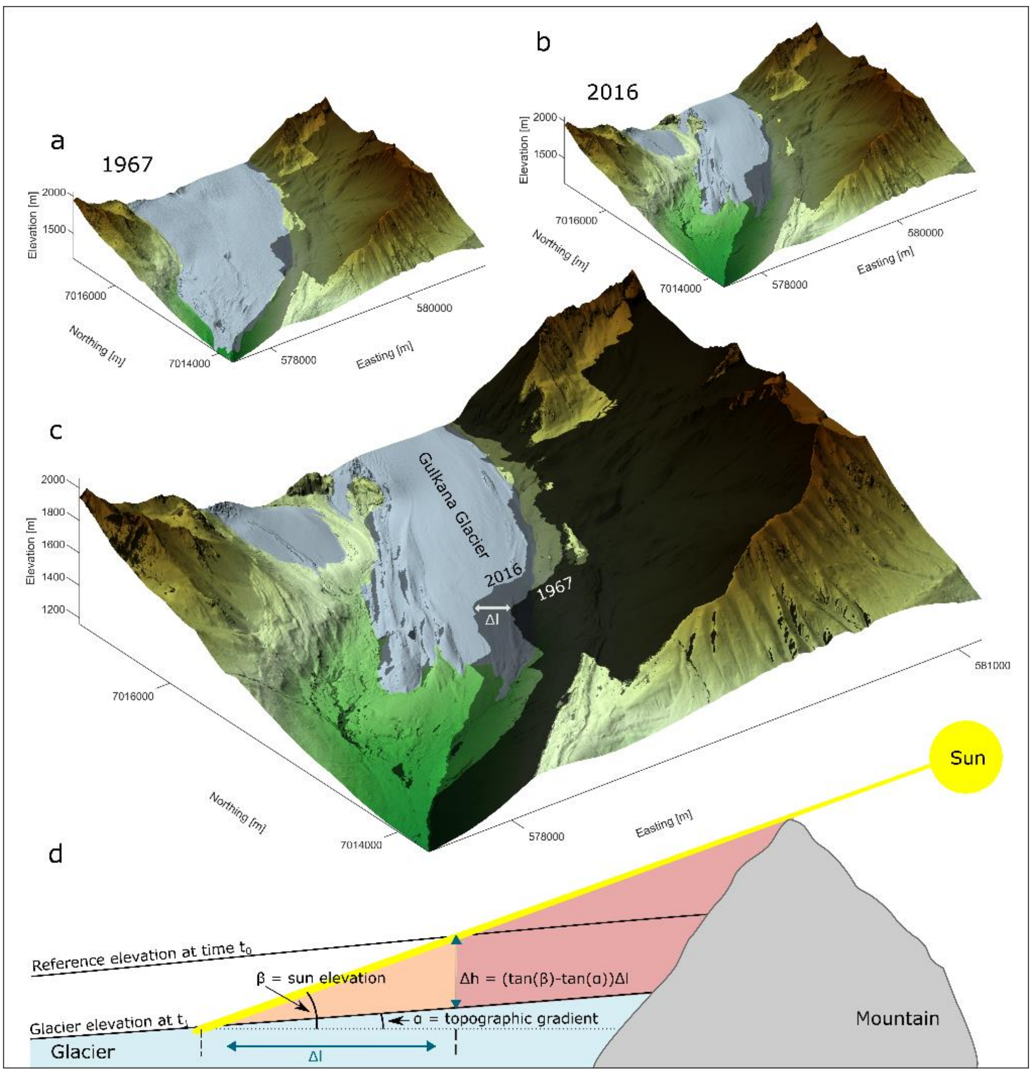

Figure 1: Effects of changing glacier elevation on the length of cast shadows. Example of modelled shadows on Gulkana Glacier, Alaska, using digital elevation models and mapped glacier outlines in two distinct years from McNeil et al (2022). **a,** DEM from, and surface area (light blue) of, Gulkana Glacier in 1967. **b,** DEM from, and surface area of, Gulkana Glacier in 2018. **c**, DEM from 2018 with shadows from 1967 and 2018. Shadows were calculated based on a sun elevation of 20° and sun azimuth of 135°. The horizontal difference between the shadows (arrow in **c**) is 210 m. **d,** Diagram of the trigonometric relationship that predicts longer horizontal shadows under a constant sun elevation β and mountain topography, assuming that the glacier maintains its topographic gradient α. In the example, the gain in shadow length at the terminus of the Gulkana Glacier translates into a glacier elevation change of ca. -76 m.

Few studies have explored the potential of ~~Previous studies that use single-look imagery together with~~ cast shadows in satellite images to detect ~~glacier elevation~~surface changes of glaciers~~are scarce~~. ~~One~~ A recent ~~attempt~~ study assessed ice-shelf freeboard heights and the height of volcanic plumes (Rada Giacaman 2022). ~~A recent study~~Another appraisal assessed ~~also investigated~~ the potential of the method for the Aletsch Glacier using Sentinel-2 for the period 2017-2021 (Dematteis et al. 2023). Yet, the potential of ~~the shadow-height~~cast-shadows ~~method~~ in glacier geodetic surveys has remained unaddressed on a broader geographic range and over longer time scales. Here we address the question of how well, or if at all, we can measure ~~topographic~~ elevation changes on glaciers based on the variability of shadows cast by surrounding mountains. To this end, we develop and test an approach that applies trigonometry to time series of shadows extracted from Landsat satellite images from 1986~~95~~ to 2021~~0~~, draped over local DEMs, in order to identify local glacier surface changes. We validate this method at five glaciers for which we have detailed information on local mass-balance and topographic changes.

2 Study sites

We selected ~~five~~ glaciers in North America, Europe, and Central Asia, spanning 20° of latitude (Fig. 2). Our selection was guided by the availability of ~~long (~~decadal~~)~~ time series of glacier mass balances and~~,~~ high-resolution DEMs, and glacier outlines, providing a validation to our analysis. The shadows cast on these glaciers account for varying sun angles and surrounding relief, and occur in accumulation as well as ablation areas.

The Great Aletsch Glacier is located in the Swiss Alps, offering one of the longest consecutive records of mass balances in this mountain region (Bauder et al. 2007). The summit of Dreieckhorn casts a pronounced shadow on the Great Aletsch Firn at ~2,950 m a.s.l., which is close to the estimated equilibrium line altitude (ELA) of 2,961 m during the period of 1971-1990 (Zemp et al. 2007). High and steep mountains surround Baltoro Glacier in Pakistan. The Mitre Peak creates a nearly triangular shadow near Concordia (~4,500 m a.s.l.), which is the confluence of Baltoro and Godwin-Austen Glacier. This shadow is likely in the ablation zone, given an ELA at ~5,200 m a.s.l. (Minora et al. 2015). The northern-most glacier in our study is Gulkana Glacier (Alaska, USA), shaded ~~twice~~ by Ogive Mountain at ~1,850 m a.s.l. in the west and by Icefall Peak at ~1,800 m a.s.l. in the east. We did not study the shadow near the tongue of Gulkana Glacier, given that most Landsat images are acquired at noon when shadows are absent or very small. The ELA of Gulkana Glacier ranged from 1,811 m a.s.l. to 2,178 m a.s.l. between 2009 and 2019 (McNeil et al. 2022), ~~such~~ so that the shadows were largely in the ablation zone. On South Cascade Glacier (Washington, USA), ~~the shadow of~~ Lizard Mountain ~~shows~~ has two peaks, which form one coherent shadow on the glacier (~2,050 m a.s.l.). This shadow is above the ELA, which ranges between 1,794 and 2,042 m a.s.l. (1986 to 2018) (McNeil et al. 2022). Finally, Sperry Glacier (Montana, USA) is shad~~ow~~ed at an altitude of ~2,350 m a.s.l. by Gunsight Mountain. The shadow is situated largely in the ablation zone, given an average ELA at ~2,500 m a.s.l. for the period 2005-2019 (McNeil et al. 2022).

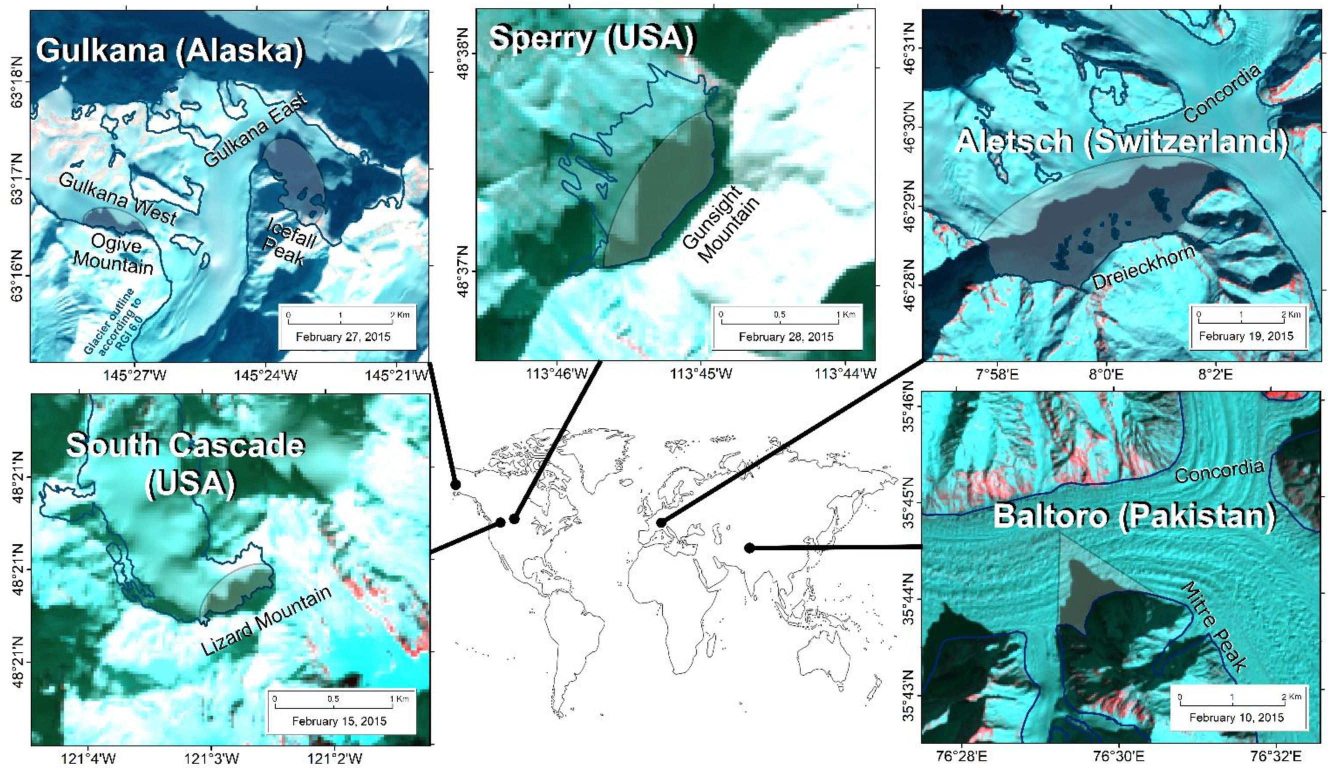

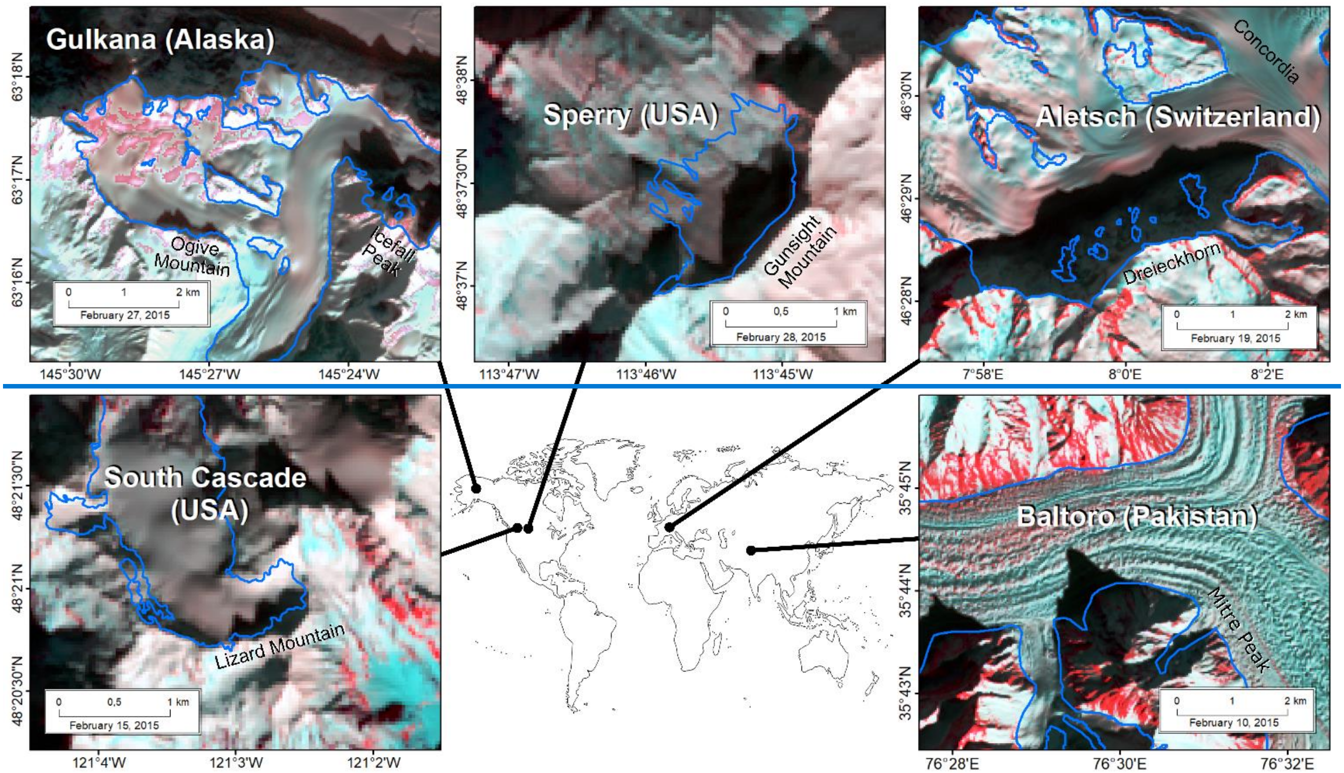

Figure 2: Map of the five study regions. Images are false-color composites (SWIR, blue, and green bands) from Landsat OLI obtained in February 2015. Blue outlines are glaciers in the Randolph Glacier Inventory (RGI), V6.0. The semi-transparent areas are approximate outlines of the shadows, which we use for comparison with independent data and studies.

3 Data and methods

3.1. Satellite images and DEMs

We obtained 30-m resolution Landsat images (level L1TP-Precision and Terrain corrected) to map shadows within the glacier surface. To this end, we downloaded 69~~0~~ cloud-free Landsat images (45~~1~~ from TM, two from ETM+, and 22~~17~~ from OLI) with acquisition period between 1986 and 2021~~0~~ from the USGS *EarthExplorer* (https://earthexplorer.usgs.gov/, Appendix A1). L1TP images offer high radiometric and geodetic accuracy by using ground control points and correcting for topographic displacement using regional DEMs (https://www.usgs.gov/landsat-missions/landsat-levels-processing#L1TP). We could not find any notable offsets between successive images.

We used several DEMs (see Table A2) to simulate cast shadows for the dates at which the Landsat images were acquired. For four glaciers, we used the DEM of the Shuttle Radar Topography Mission (SRTM-1), which has a spatial resolution of 30 m (Farr et al. 2007). ~~For~~ Gulkana Glacier is located beyond the maximum acquisition range of SRTM at 60°

North.~~,~~ ~~we~~ We therefore used ~~the~~ a 2-m stereo-photogrammetric DEM of WorldView-1 data acquired in 2009, which is also part of the ArcticDEM. ~~(acquisition year 2009, 2 m spatial resolution) given that this glacier is located beyond the maximum acquisition range of SRTM at 60° North.~~ Owing to high vertical uncertainties in SRTM data in rough topography (Mukul et al. 2017; Liu et al. 2019), we ~~also~~ used ~~a number of other~~additional DEMs to enhance and validate our results. For Great Aletsch Glacier, we obtained the swissALTI3D DEM (acquisition year 2017-2018, version 2019, downsampled to 5 m spatial resolution by merging multiple raster datasets). For Baltoro Glacier, we ~~modified the SRTM-1 so that the mountains are~~ replaced the ~~with data~~mountains in the SRTM-1 DEM using data from the Viewfinder Panoramas (VFP) project (De Ferranti 2015). VPF is an improved~~data mainly consists of SRTM data but has been filled and corrected~~ version of the SRTM DEM drawing on auxiliary DEMs at locations ~~with other sources~~ where SRTM features voids or artefacts due to phase unwrapping errors ~~within the SRTM data occur~~. In the Higher Himalayas, the accuracy of the SRTM DEM decreases as elevation and steepness increase (Mukul et al. 2017, Liu et al. 2019). Indeed, the original SRTM-3 DEM features a void at Mitre Peak, and suggests that its elevation was interpolated (EROS 2018). We found that VFP is most suitable to cast shadows onto Baltoro Glacier (https://doi.org/10.5194/tc-2022-194-AC1), and~~We~~ therefore ~~merged both DEMs~~filled this void using VFP data while ~~because we wanted to~~ maintaining~~keep~~ the elevation of the glacier from the original SRTM DEM ~~as its survey date is known to be the year 2000, while the date of the map basis of VFP is not known to us~~. ~~The~~ We assume that the ~~latter~~ unknown acquisition date of VFP has little impact on our subsequent analysis as Mitre Peak is free of glacier ice and no major rockfalls were reported during our study period that could have reduced its elevation~~because we assume the elevation of mountain ridges to remain unchanged during our study period~~.

3.2. Workflow for estimating trends in glacier elevation change in shaded areas

We created a binary mask of shaded and non-shaded areas (Fig. 3a) by applying a user-defined threshold to the digital numbers of the green band (encompassing a wavelength of 525-600 nm) of each Landsat scene (Appendix A1). We found the green band suitable because shadows appear dark on the otherwise bright glacier surface. Snow, firn, and ice have minimal absorption in the blue-green range, whereas red and infrared light is strongly absorbed on these surfaces. This trait enhances contrast at the interface of glaciated surfaces and shaded, colder areas with increasing wavelength. Incoming and reflected electromagnetic wavelength in the green band is also less affected by the Rayleigh scattering in the atmosphere compared to the blue band that has a shorter wavelength. The green band therefore offers a good compromise between contrast and surface reflectance measured at the sensor, and has been successfully used in mapping glacier outlines (Paul et al. 2016). For each Landsat image, we obtained the sun azimuth and sun elevation from the associated metadata file. We used these two parameters ~~of the sun position~~ to simulate cast shadows using a ray-tracing algorithm ~~available~~ implemented in SAGA-GIS V2.3.2 (Conrad et al. 2015). This algorithm returns a binary raster classifying each pixel either as shaded or non-shaded, equivalent to our threshold-based mapping (Fig. 3b). We then calculated the difference in area between the modelled shadow and

~~manually mapped shadow~~shadow derived from Landsat images.~~,~~ ~~and~~ We clipped the resulting polygons to the glacier outline in the Randolph Glacier Inventory (RGI) V6.0 (Pfeffer et al. 2014) (Fig. 3c). Within these difference polygons, we obtained the change in shadow length using ~~geodetic~~ bearing lines at a regular horizontal spacing of 30 m (i.e. the cell size of Landsat images) in the direction of the sun azimuth (Fig. 3d–f, Appendix A1). These lines represent the incoming sun rays and are assumed to be parallel, given that the Sun is a distant, point-shaped light source. Thus, ~~and~~ the change in shadow length is considered relatively short compared to the distance between Earth and Sun. Artefacts in the ~~geodetic~~ bearing lines (Fig. 3d) appeared mainly because of the limited resolution of the DEM and satellite images (i.e. ~~interruption of~~interrupted lines by pixel corners or shadow bottom edge and hole phenomenon), ~~such that~~so we removed them manually. Finally, we used the trigonometric relationship of the law of tangents to convert the length of each line to changes in elevation relative to the date when the DEM was acquired (Fig. 1). Earth curvature could influence the length of the simulated shadows and thus the glacier elevation changes, albeit only in the millimetre range, and is therefore not considered in our analysis.

We have scaled the elevation changes for each glacier so that the median for the year 2000 is zero, because in most cases the data are relative to the elevation values in the SRTM DEM from February 2000. The changes in glacier elevation in the other years are therefore the positive or negative deviations from the median in 2000.

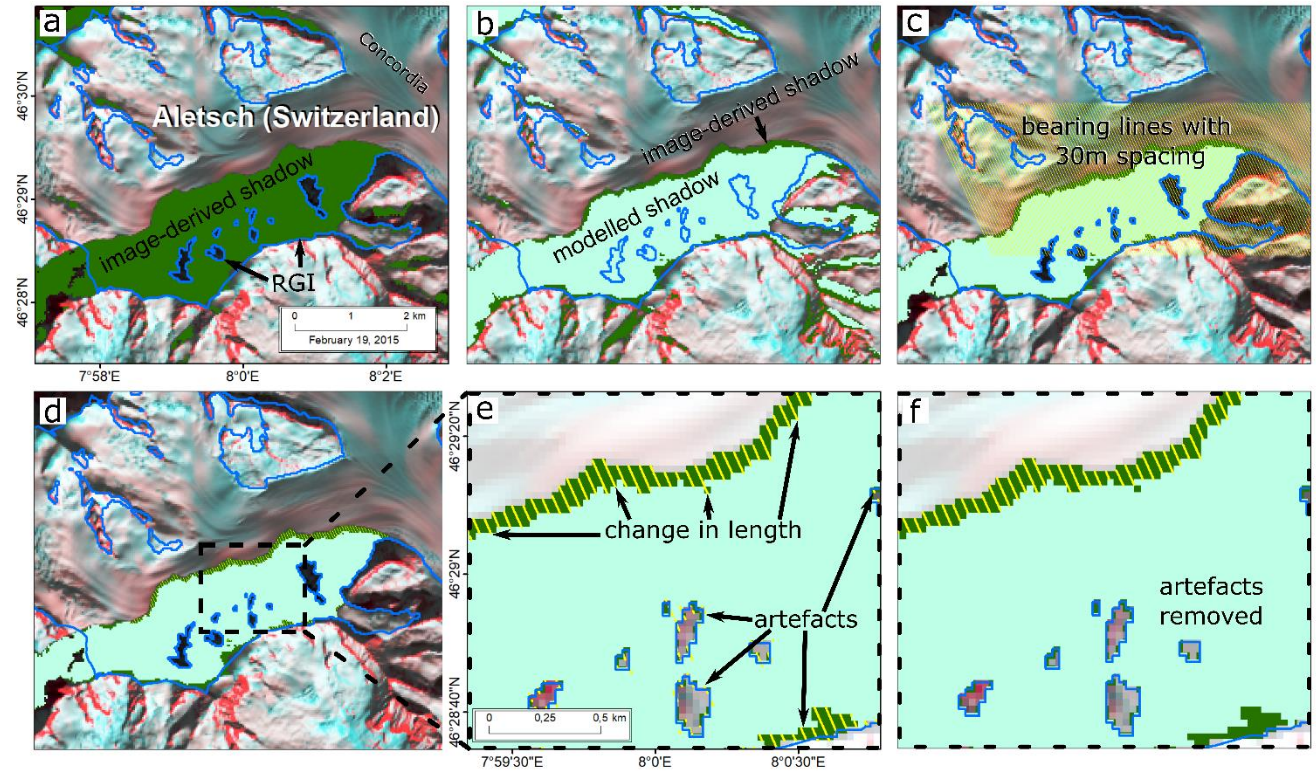

a
b
c
d
e
f
Concordia
Aletsch (Switzerland)
image-derived shadow
RGI
0 1 2 km
February 19, 2015
46°30'N
46°29'N
46°28'N
7°58'E
8°0'E
8°2'E
image-derived shadow
modelled shadow
bearing lines with
30m spacing
change in length
artefacts
0 0,25 0,5 km
46°29'20"N
46°29'N
46°28'40"N
7°59'30"E
8°0'E
8°0'30"E
artefacts
removed

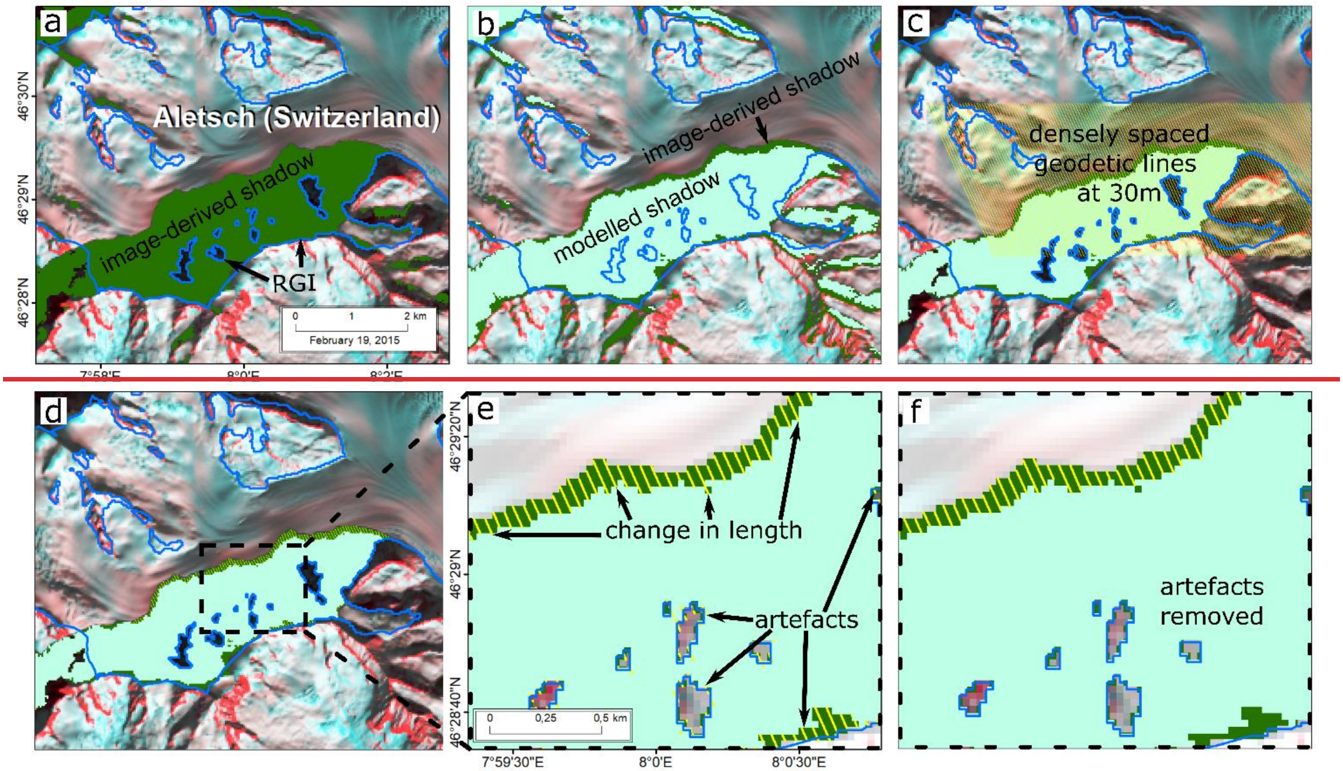

Figure 3: Flowchart of modelling terrain shadows using the example of Great Aletsch glacier. (a) ~~Shadows mapped~~Mapped shadows (green) using a threshold of 5,500 in the Landsat 8 image (using false-color composite in the SWIR, blue, and green bands) together with ~~Randolph Glacier Inventory (~~RGI~~)~~, **(b)** Modelled shadow (turquoise) using SAGA-GIS, draped over the mapped shadow in the Landsat image, **(c)** Extracted shadows by RGI and pattern of parallel ~~geodetic~~ bearing lines, **(d)** Lines cut to the difference between the two shadows, **(e)** Close up of d with generated lines of change in shadow length and unwanted artefacts, **(f)** Artefacts at the bottom edge and along cut outs are removed.

We used a Bayesian multi-level linear regression model to estimate ~~the~~ linear trends in elevation change for each glacier with time. Multi-level models can accommodate groups in data, in our case different glaciers, within a single model. We can thus estimate local effects at a given glacier with respect to the entire population learned from all data regardless of their location. Multi-level models improve parameter estimates for individual groups, in particular when differing sample sizes cause variance across the groups (McElreath 2020). Multi-level models are suitable for datasets with a different sample sizes in each group. In our case glacier, one glacier might have hundreds of bearing lines (e.g. Great Aletsch Glacier) in a given year and others might have fewer data (e.g. the eastern shadow of Gulkana Glacier). The hierarchical model structure avoids over-fitting parameters for glaciers with many bearing lines and generally improves inference for groups with few data points. ~~This feature is advantageous in our analysis as the number of geodetic~~ bearing ~~lines per year differs strongly among glaciers. The model learns the population-level parameters from the data, which serve as shared prior distributions for each group. In this~~

~~way, t~~The glaciers inform each other, given that groups are conditioned on the data from all glaciers, reducing uncertainty in years with few ~~geodetic~~ bearing lines at a given glacier. The parameters in the model are drawn from distributions specified by population-level (hyper-) parameters, which are also learned from the data. The multi-level model returns the posterior distribution for both population-level and group-level parameters.

Our likelihood function follows a Student's t-distribution, which is robust against outliers (Kruschke 2014). We modelled the trend in glacier elevation change Δh with year y as

$$\Delta h_{ji} \sim t(\mu_{ji}, \kappa, \nu), \text{ for } j = 1, \ldots, J \text{ and } i = 1, \ldots, n_j \quad (1)$$

$$\mu_{ji} = \alpha_j + \beta_j y_{ji}, \text{ for } j = 1, \ldots, J \text{ and } i = 1, \ldots, n_j \quad (2)$$

$$\begin{bmatrix} \alpha_j \\ \beta_j \end{bmatrix} \sim MVNormal\left[\begin{pmatrix} \alpha \\ \beta \end{pmatrix}, \boldsymbol{S}\right] \quad (3)$$

$$S = \begin{pmatrix} \sigma_\alpha & 0 \\ 0 & \sigma_\beta \end{pmatrix} R \begin{pmatrix} \sigma_\alpha & 0 \\ 0 & \sigma_\beta \end{pmatrix} \quad (4)$$

$$R = \begin{pmatrix} 1 & \varsigma \\ \varsigma & 1 \end{pmatrix} \quad (5)$$

where Δh are the elevation changes from ~~geodetic~~ bearing lines in each year, i is an index for n ~~geodetic~~ bearing lines, and J is the number of glaciers. The likelihood function has a location parameter μ, κ is a positive scale parameter, and ν are the degrees of freedom, fixed at $\nu = 3$. The parameters α_j and β_j are the intercepts and slopes for each group, respectively, and α and β are the corresponding parameters on population-level. The covariance matrix S is composed of group-level standard deviations σ_α and σ_β, and R, the correlation matrix with correlation ς. We choose the following priors to model the parameters for the entire population and all groups (i.e. the glaciers)

$$\kappa \sim N(0, 2.5) \quad (6)$$

$$\alpha \sim N(0, 2.5) \quad (7)$$

$$\beta \sim N(0, 2.5) \quad (8)$$

$$\sigma_\alpha \sim N(0, 2.5) \quad (9)$$

$$\sigma_\beta \sim N(0, 2.5) \quad (10)$$

$$R \sim L\sout{kj}KJ\,Cholesky(1). \quad (11)$$

These priors refer to standardised data pairs (Δh and y) with zero mean and unit standard deviation. Choosing wide priors with a zero-mean Gaussian and standard deviation of 2.5 admits both negative and positive trends for β, such that the posteriors are largely informed by the data. We choose a Lewandowski–Kurowicka–Joe (LKJ) Cholesky~~Cholesky LKJ~~ correlation distribution prior for R, so that all correlation matrices are equally likely. We numerically approximate this posterior using a Hamiltonian sampling algorithm implemented in `Stan` that is called via the software package `brms` within the statistical programming language `R` (Bürkner 2017; R Core Team 2022; Stan Development Team 2022~~; R Core Team 2022; Bürkner 2017~~). We ran three parallel chains with 6,000 iterations after 2,000 warm-up runs, and found that the Markov chains have converged ($\hat{R}$ statistic = 1.0). We report the posterior distributions of all model parameters in Table A3.

3.3 Comparison to reference DEMs and historical maps

~~The density of ice in shaded areas remains unknown, so we refrained from converting our data to water equivalents. Instead, w~~We compared our estimated trends in glacier elevation change with trends ~~calculated~~ from multi-temporal, high-resolution DEMs in shaded areas~~for the same shaded areas~~. For all glaciers in North America, we used repeated DEMs available for USGS benchmark glaciers ~~(from~~ McNeil et al. ~~(~~(2022). These ~~and sampled the elevation values in polygons covering the areas around the shadow outlines. These~~ DEMs~~S~~ have spatial resolutions ranging between a few decimeters to 10 m, and were derived from historic topographic maps, aerial stereo photography, and space-borne imagery. For all DEMs, we extracted the mean elevation change within a simplified silhouette, which remains constant with time, given that the shape of the shadows varies due to changing acquisition dates and sun angles. For the Great Aletsch Glacier, we obtained glacier elevation changes from ~~online~~ historical maps (~~Siegfriedkarte~~ Landeskarte ~~with reference system 1903~~ at map scales of 1:25,000 and 1:50,000) available for 12 years between 1959 and 2020 from the Bundesamt für Landestopografie KOGIS (Koordination, Geoinformation und Services, https://www.swisstopo.admin.ch). Mountain peaks in these maps are labelled with elevation values and we consider them as stable terrain in the past 60 years. A sample of 10 peaks suggests positive and negative offsets of less than 5 m compared to the high-resolution SwissALTI3D DEM, making them suitable for validating our method over a period of more than six decades (Fig. A1; Table A5). To infer elevation changes from contour lines in historical maps, we manually chose four points with a spacing of 1 km along a straight line in the flow direction of the glacier within the area covered by the shaded glacier (Fig. A1). For each map, we then extracted the glacier elevation at each point using linear interpolation and calculated the average elevation change from these points. ~~For~~ We could not find any historical elevation data for the Baltoro Glacier that would be suitable for comparison. ~~Baltoro Glacier, high-resolution historic elevation data for comparison are unavailable.~~

We use the same multi-level structure as above (Eqs. 1-11) to determine the trends in glacier elevation change from glaciers with repeat, high-resolution DEMs. To this end, we conditioned the model on J = ~~4~~ 5 ~~glaciers~~ glacier shadows (excluding Baltoro), chose the same priors, and maintained the setup of the Hamiltonian sampler. We learned two models, one with all available data and one with data limited to the Landsat period, to make trends comparable to our study period. In either case, ~~W~~we found that all chains have converged ($\hat{R}$ = 1.0) and report all model parameters in Table A4.

3.4 Comparison to glacier elevation changes from Hugonnet et al. (2021)

In addition, we compared the elevation changes of our six study glaciers with time series from Hugonnet et al. (2021). In their study, the entire archive of satellite images from the Advanced Spaceborne Thermal Emission and Reflection Radiometer (ASTER) mission was automatically assembled into DEMs, stacked and co-registered with other DEMs from the Arctic-DEM at a spatial resolution of 100 m x 100 m. In general, each pixel is covered by several dozen DEMs over the period 2000 and 2019. Noise and artefacts in the DEMs that would lead to excessively strong rates of glacier elevation change are iteratively filtered from the time series by several fixed thresholds, deviations from the reference TanDEM-X DEM, as well as by a Gaussian Process (GP) regression. Unlike our linear regression model, the GP regression model allows for seasonal, periodic oscillations in glacier height, so that the interpolated time series of glacier elevation change shows a sinusoidal up and down. We thank Romain Hugonnet for extracting time series of glacier elevation change within simplified outlines of glacier shadows (Fig. 2) and for providing summary statistics on mean glacier elevation change between 2000 and 2019 (Fig. 6). For comparison, we shortened our dataset to cover the same period and fitted the Bayesian hierarchical model with the same structure and parameterisation as above.Brief description of Hugonnet's assessment.

Hugonnet et al. (2021) produced time series of automatically generated DEMs from the Advanced Spaceborne Thermal Emission and Reflection Radiometer (ASTER) satellite mission between 2000 and 2019. Similar to our assessment, Hugonnet et al. (2021) estimated cumulative and mean rates of glacier elevation change in this period from a number of DEMs per glacier using stereo-photogrammetry.

Consistent comparison with data from Hugonnet, both for entire glacier, and shadow area. That paper is the global benchmark now, available for every glacier on Earth.

Used GP regression.

To this end we merged the shaded area from all observations, then romain extracted the elevation change as described in his paper.

Use data only for 2000 – 2019

3.54 Assessment of cast -shadows from globally available DEMs

We assume that tThe choicquality of the of the DEM couldmay bias our estimates of glacier elevation changes due tobecause the DEMs can have different spatial resolutions, artefacts, and horizontal and vertical errors (e.g. due to foreshortening, layover, and shadow effects) characteristic for different DEM sources. These uncertainties propagate into modelled cast -shadows and likely affect possible trends in glacier elevation derived from different globally available DEMs

(Table A2). The Great Aletsch Glacier provides six several freely available DEMs, which we used to quantitatively and qualitatively assess changes in the size and shape of the inferred shadows. From Open Topography (https://opentopography.org/), we obtained two SRTM DEMs (SRTM-1 with 30 m and SRTM-3 with 90 m spatial resolution), the NASADEM (~~30 m,~~ a reanalysis of SRTM data with 30 m resolution), ALOS World 3D (AW3D30 with 30 m), and two Copernicus DEMs (GLO-30 with 30 m and GLO-90 with 90 m). We compared the DEM-derived shadows to those from the LiDAR-based swissALTI3D DEM, which we treat as the benchmark. In each simulation, we use a sun azimuth of 135° and sun elevation of ~~30~~25°.

Finally, ~~Moreover, in addition to the swissALTI3D data, we conducted the analysis for all Landsat-derived shadows for the SRTM-1 and GLO-90 DEMs to~~ we also studied ~~y the effect of chang~~the role of the DEM~~ing~~ resolution~~s~~ in our method~~on temporal trends of glacier surface elevation~~. In theory, choosing a coarser DEM resolution than Landsat (30 m) could lead to higher noise in our method, as one DEM pixel is represented by several Landsat pixels. To this end, we calculated the difference between the shadow mapped from Landsat images and the shadow simulated from three input DEMs. Taking the Great Aletsch Glacier as an example, we compared the variance of elevation change with time using bearing lines drawn through the s~~S~~wissALTI3D DEM (5 m, highest resolution), the SRTM-1 (30 m, medium resolution, corresponding to that of the Landsat images) and the GLO-90 DEM (90 m, lowest~~highest~~ resolution).

4 Results

4.1 Glacier elevation changes from cast shadows

In each Landsat scene, $31^{+79}/_{-11}$ ~~geodetic~~ bearing lines (median, 2.5%, and 97.5% of the distribution) with a regular spacing of 30 m between each line pass through the mapped shadows on the five selected glaciers (Appendix A1). Individual ~~geodetic~~ bearing lines suggest the lowest variance in glacier elevation change at Sperry Glacier (-22 m to +5 m; 2.5% and 97.5% of the distribution) and the highest variance at Gulkana West (-94 m ~~/~~to +30 m), when adjusting elevation changes relative to the year 2000. Our analysis of trends in glacier elevation changes suggests that Gulkana West and Great Aletsch Glacier had the highest annual rates of thinning of $-1.21^{+0.15}/_{-0.16}$ and $-1.08^{+0.05}/_{-0.05}$ m yr^{-1}, respectively (mean and 95% highest density interval, HDI). The mean elevation change in the western, lower-lying arm of Gulkana Glacier is about 10 times that of the eastern, higher-lying arm. Sperry and South Cascade Glacier lost on average about 0.4 m per year since the late 1980s. The eastern arm of the Gulkana glacier has been thinning at a credible negative, albeit low, annual rate, while the surface of the Baltoro glacier had no change in recent years~~.~~ (Fig.~~ure~~ 4).

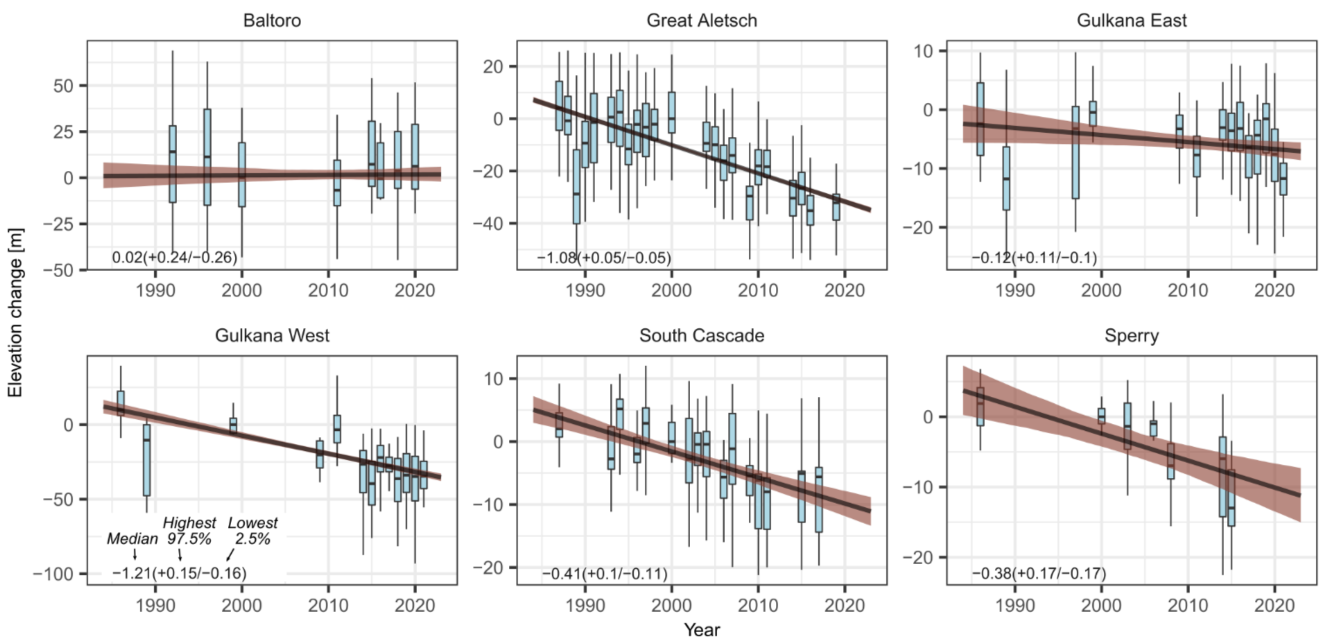

Figure 4: Trends in mean elevation change on shaded glacier surfaces. Boxplots show annual glacier elevation changes, which we have derived from bearing lines drawn through shadows in Landsat images. Values of elevation change are relative to ~~the reference year, i.e.~~ the ~~year~~ median value in ~~of DEM acquisition~~2000 (for Gulkana in 1999). ~~Horizontal lines are the median, b~~Boxes encompass the interquartile range, ~~and~~ whiskers are 1.5 times the interquartile range, and horizontal lines are the median. Outliers (lowest and highest percent in the distribution) are removed. Thick black line is the mean posterior trend and brown shade is the 95% highest density interval (HDI). Numbers in lower left corner summarise the posterior distribution of the trend in glacier elevation change, including the median, the lower 2.5%, and the upper 97.5% of the HDI.

4.2 Comparison with reference DEMs

Our estimated trends from ~~geodetic~~ bearing lines match the trends obtained from high-resolution DEMs and historical maps (Fig. 5). However, uncertainties in the trends calculated from the reference DEMs are consistently higher given that fewer data enter the hierarchical regression model, especially if we fit the model only to data obtained during the shorter Landsat period. At Great Aletsch Glacier, we find similar trends in mean glacier elevation change between our method ($-1.08^{+0.05}/_{-0.05}$ m yr^{-1}) and the ~~high-resolution DEMs~~reference DEMs both since 1959 ($-1.06^{+0.27}/_{-0.31}$ m yr^{-1}) and during the Landsat period ($-0.88^{+0.49}/_{-0.76}$). At South Cascade Glacier, the mean trend from the high-resolution DEMs is more than twice that of the trends obtained from ~~geodetic~~ bearing lines ($-1.06^{+0.54}/_{-0.45}$ vs. $-0.41^{+0.1}/_{-0.11}$ m yr^{-1}). Trends are more consistent, however, if we consider all available data from South Cascade, extending back to late-1950s (Fig. 5). ~~At~~ For the two shadows at the Gulkana glacier, the mean trends from the DEMs during the Landsat period are negative and midway between the very high and low values that we had determined for the two arms. ~~Gulkana, both our method and high-resolution DEMs suggest the highest uncertainties in the estimated trends, leaving little room for a credible trend in glacier elevation change.~~Trends in historical DEMs ~~Note the large uncertainties at Sperry Glacier~~are difficult to determine at Sperry Glacier~~, given that~~ because only two observations inform the multi-level model during the Landsat period.

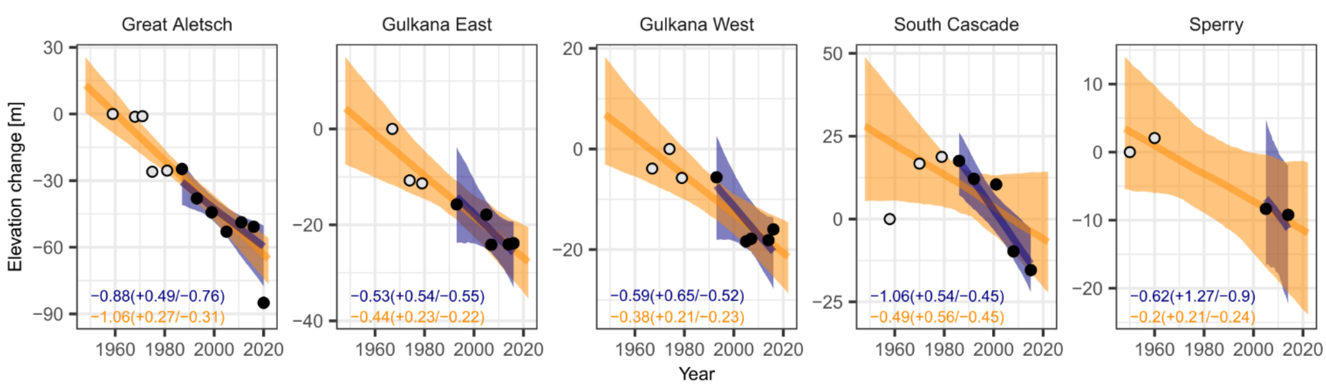

Figure 5: Reported glacier elevation changes in shadowed areas for four glaciers. All values are relative to the first observation for each glacier, which is set to zero. Black bubbles are observations when Landsat images are available for a given glacier (see trends in Fig. 4). G~~,~~ ~~g~~rey bubbles mark data~~values~~ obtained before the Landsat period~~ (meaning they were derived from sources like the USGS survey, the historical map – Landeskarte, etc., as indicated in L184)~~. Shades, thick lines, and numbers refer to models fit to all data from ~~the Landsat period (blue) and pre-Landsat~~ the entire period (orange), and to data for the Landsat period only (blue). Numbers in lower corner left summarise the posterior distribution of the annual trend in glacier elevation change, including the median, the lower 2.5%, and the upper 97.5% of the HDI.

4.3. Comparison with data from Hugonnet et al. (2021)

If we reduce our study period to 2000-2019, we find that our trends generally follow those of Hugonnet et al. (2021). The exception is Gulkana West, where our estimated mean rate of glacier thinning is more than twice as high. The most negative, though credibly different, trends occurred at the Great Alettesch Glacier. In all other cases, the trends of the two data sets overlapped. One reason for the discrepancy between the two datasets may be the rigorous filtering of outliers in the dataset of Hugonnet et al. (2021), whereas in our method we retain the elevation changes of all bearing lines, regardless of their distances from the mean or median.

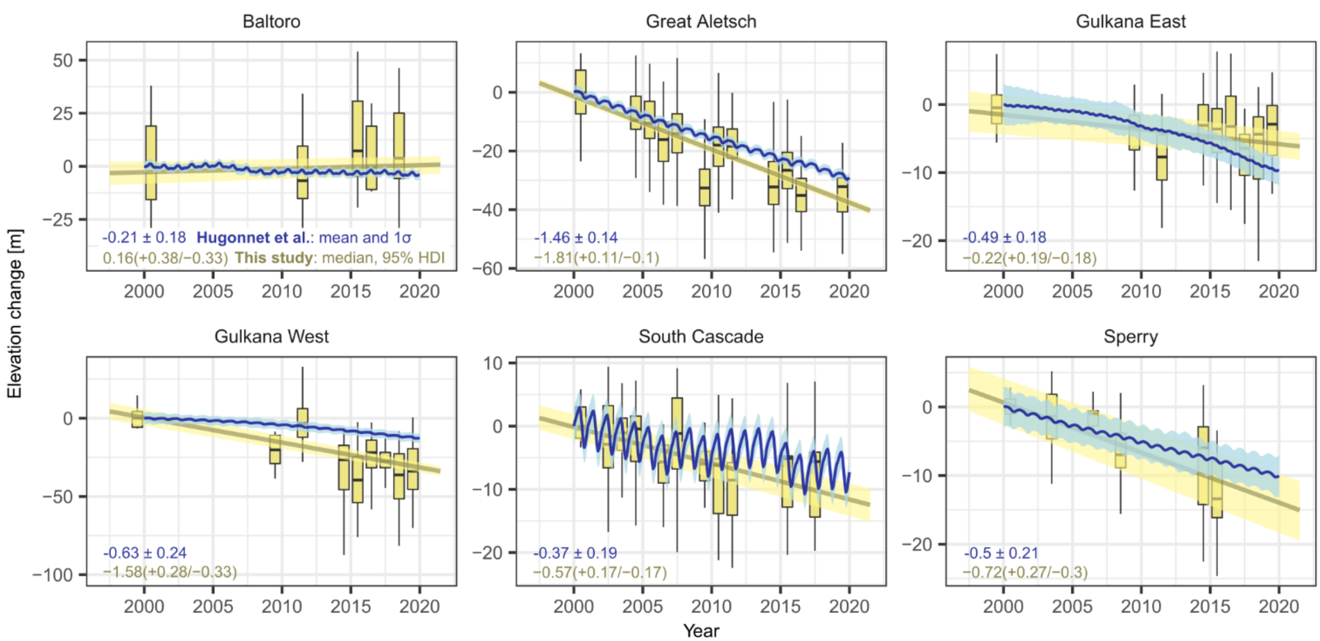

Figure 6: Glacier elevation changes in shaded areas using our method and that of Hugonnet et al. (2021) between 2000 and 2019. All values are relative to the year 2000, which is set to zero. Yellow Green colors refer to our method, and blue colors are trends of glacier elevation change using Gaussian Process (GP) regression through time series of ASTER DEMs from Hugonnet et al. (2021). Boxes encompass the interquartile range, whiskers are 1.5 times the interquartile range, and horizontal lines are the median. Outliers (lowest and highest percent in the distribution) are removed. Thick yellowgreen line is the median posterior trend and lightyellowgreen shade is the 95% highest density interval (HDI). GreeYellown number in lower left corner is our posterior estimate of the annual trend in glacier elevation change, including the mean, the lower 2.5%, and the upper 97.5% of the HDI. Blue number is the mean annual trend and 1σ error from Hugonnet et al. (2021).

Table 1: Comparison of trends in glacier elevation change [m yr^{-1}] between this study and that of Hugonnet et al. (2021). Trends were obtained from data in the period 2000 and 2019.

Glacier	This study	Hugonnet et al. (2021) – entire glacier	Hugonnet et al. (2021) – shadow area only

~~Great Aletsch~~	-	-	-
~~Gulkana North~~	-	-	-
~~Gulkana South~~	-	-	-
~~South Cascade~~	-	-	-
~~Sperry~~	-	-	-
~~Baltoro~~	-	-	-

-

4.4 Influence of DEM type and resolution

We conducted the shadow-based detection of glacier elevation changes with three DEMs for the Great Aletsch (Fig. 7). The length of bearing lines between shadows (and derived elevation changes) scatters substantially, but the shapes of nonparametric regression curves are ~~highly~~ consistent between the different DEMs. Apart from these trends, residuals from these trends are affected by the underlying DEM ~~used~~. R~~While r~~esiduals of the SRTM-1 and GLO-90 had~~show~~ a high standard deviation of 18.2 m and 26.8 m. R~~, r~~esiduals are lowest for ~~of~~ the s~~S~~wissALTI3D DEM at~~vary with~~ a standard deviation of 14.3 m, suggesting that an increase in DEM resolution may improve the precision of our method.~~,~~

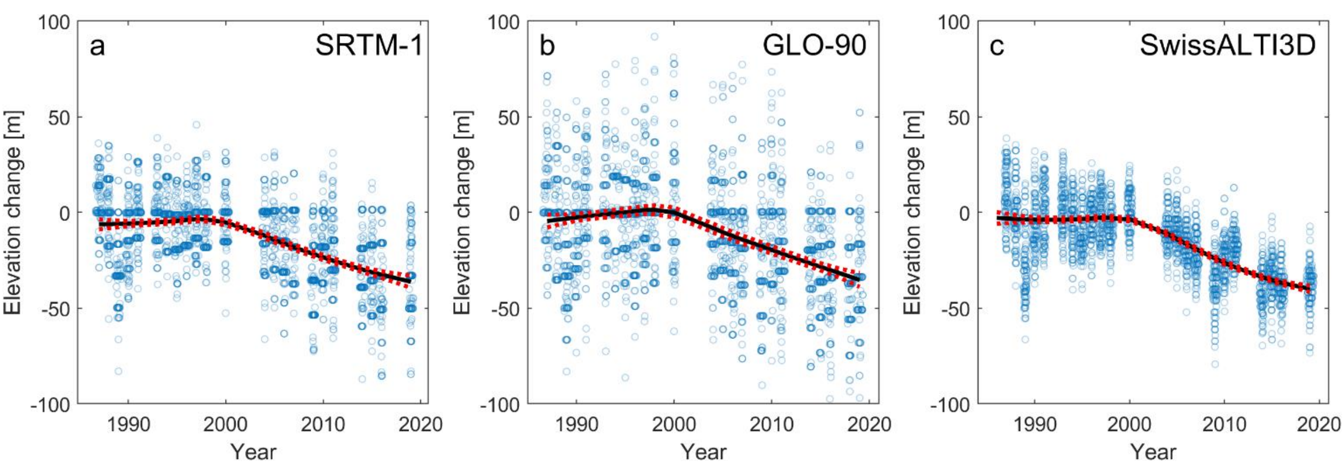

Figure 7: Glacier elevation changes of the Aletsch Glacier (see extent in Fig. 3) based on Landsat imagery and modelled shadows derived from ~~different~~three digital elevation models (DEMs). ~~Individual~~ Semi-transparent blue points show~~represent~~ the elevation change derived from the length of individual bearing lines between ~~modelled and image~~Landsat-derived shadows and those modelled form **a)** the 30-m SRTM-1 DEM, **b)** the 90-m GLO-90 DEM, and **c)** the 5-m s~~S~~wissALTI3D DEM. Black~~Trend~~ lines are the means ~~derived with~~from a lowess regression of elevation change against time. Dashed~~,~~ red lines are bootstrapped confidence intervals (±~~+/- 2~~2σ).

4.453 Comparison of shadows derived from DEMs

The elevation changes obtained from geodetic bearing lines have substantial variance in a given year (Fig. 4) despite covering a small range in elevation along the glacier. We infer, suggesting that DEM resolution and quality haveare important controls oin estimateding glacier elevation changes from cast shadows. Indeed, the example of the Great Aletsch Glacier shows that different DEMs produce shadows of different lengths, even with constant sun azimuth and elevation (Figs. 68, 79). This variation reflects limits in the DEM resolution and the representation of ridge lines. The acquisition date may also play a role, assuming that ongoing thinning might produce longer shadows in more recent DEMs. In our example, shadows projected from swissALTI3D DEM (5 m spatial resolution, acquisition in 2017 and 2018) extend farthest to the north (Fig. 6a8a). The large shadow area thus likely follows both from the reported decadal glacier thinning and from a more precise representation of the surrounding topography (Fig. 6a8a). Shadows from the GLO-30 DEM (acquisition date 20110-2015, ~30 m spatial resolution) are very similar to those derived from the swissALTI3D DEM (Figs. 6b8b, 79). We also find the smallest variance in shadow length for the GLO-30 DEM (Fig. 79). Shadows derived from the GLO-90 DEM (~90 m resolution) show both a larger spatial offset (Fig. 86c) as well as a higher variability in shadow length (Fig. 97). We attribute this mismatch to a higher degree of spatial averaging, causing lower topographic ridges due to the coarser spatial resolution. Shadows derived from the AW3D30 DEM (acquisition period between 2006 and 2011, ~30 m spatial resolution) are highly variable compared to the swissALTI3D DEM (Fig. 86d). Some of the shadows extend beyond those derived from the swissALTI3D DEM, an effect of exaggerated topography in the DEM that overestimates the height of the ridge (Fig. 97). Finally, shadows derived from the SRTM DEMs and NASADEM (Fig. 86e-g) – all derived from data acquired from the same shuttle mission in 2000 – show the highest difference to the swissALTI3D DEM. SRTM DEMs and NASADEM derived shadows are very similar, but again, the coarser SRTM-3 DEM leads to a lowering of the ridges and larger horizontal distances. In summary, variations in modelled shadows obtained from different DEMs relate to variable acquisition dates but also reflect how accurately ridge topography is represented in the DEMs. Comparison of DEMs with the same acquisition date but different spatial resolution show that coarser DEMs underestimate ridge height and commensurately shadow length. Notwithstanding, a general trend towards longer shadows and thus a trend towards lower glacier elevations can be observed for younger acquisition dates (Fig. 79).

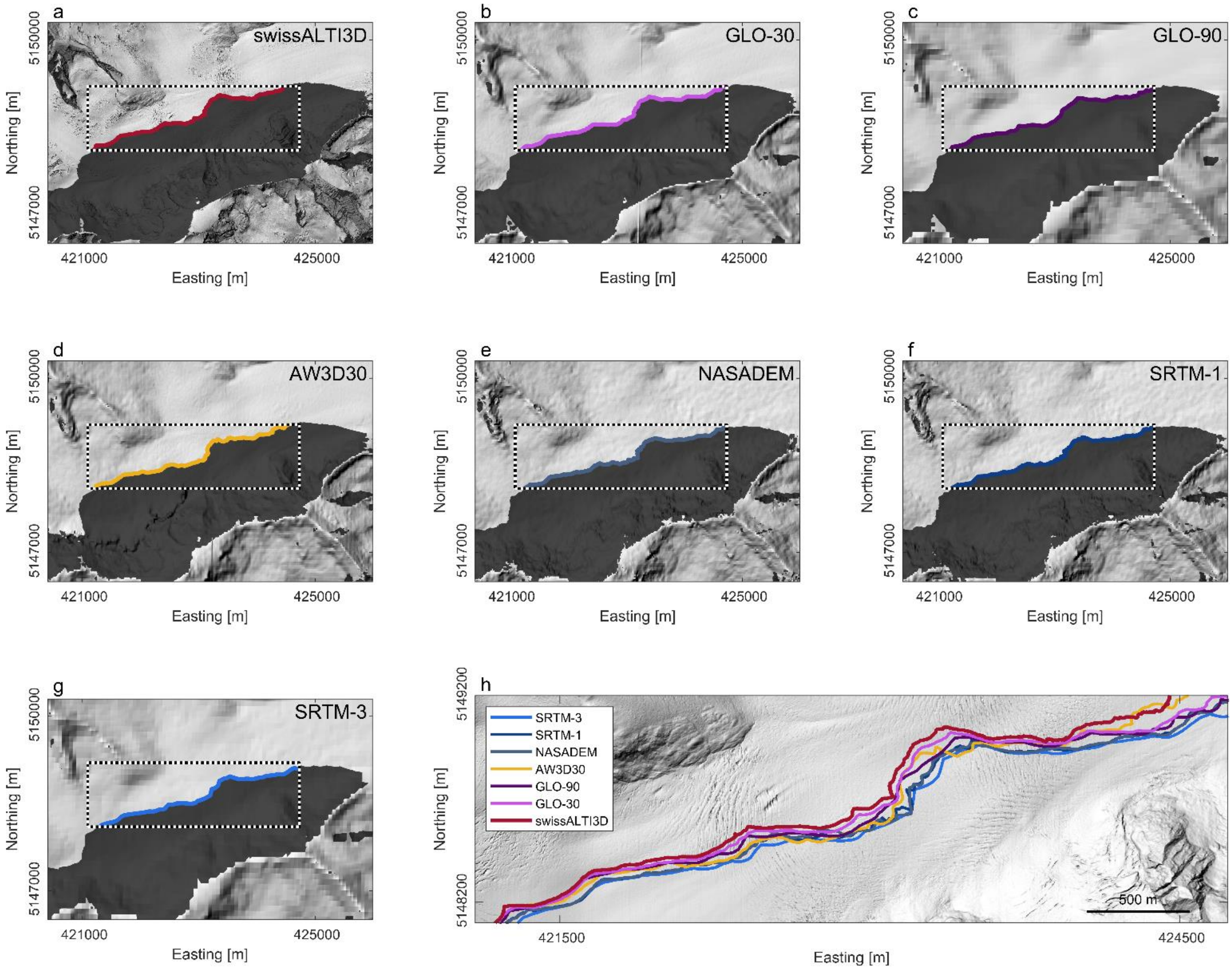

Figure ~~6~~8: Shadows projected onto Great Aletsch Glacier using different digital elevation models. (a-g) Grey hillshades show the simulated cast shadow using a sun azimuth of 135° and elevation of 25°. **(h)** Close-up of the shadow outlines modelled with different DEMs. Hillshade in the background is from the swissALTI3D DEM.

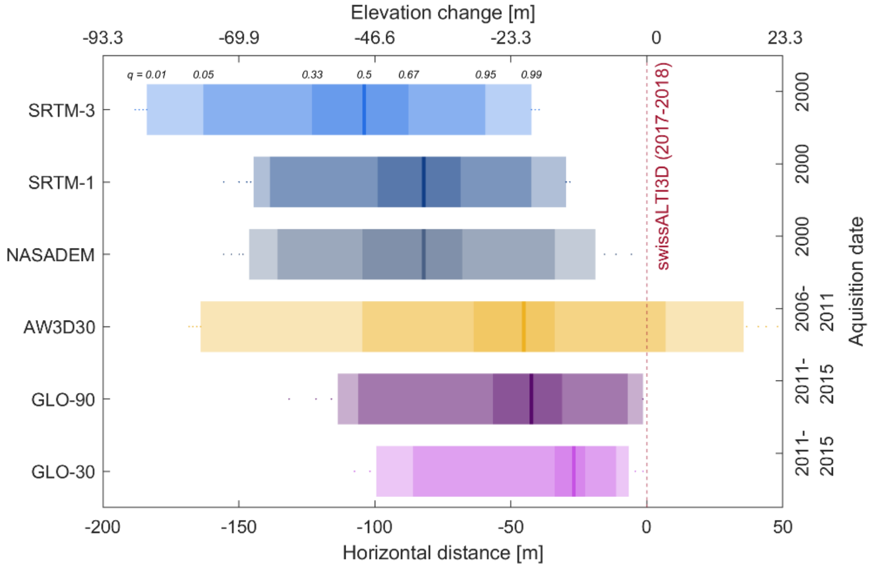

Figure ~~7~~9: Difference in the lengths of bearing~~geodetic~~ lines crossing a shadow on Great Aletsch using six DEMs and the benchmark swissALTI3D DEM.

4 Discussion

We developed and assessed a method that allows for measuring glacier elevation changes in remote areas based on shadows casted from adjacent mountains. The precision and accuracy of the method depend on several factors that pertain to the individual processing steps and the input data (Rada Giacaman 2022). We show that DEM quality and resolution cause variability in the detected elevation changes (Figs. 7-9). To this end, we assessed the length of ~~geodetic~~bearing lines that link the shadow outlines along the azimuth direction. We find that spatial resolution affects the precision and accuracy of these lines (Fig. 7). First, DEMs with coarser resolution decrease the precision due to spatial averaging, blurring ridge topography by smoothing out peaks and saddles (Purinton and Bookhagen 2017). This effect may be more pronounced in SRTM data, which can have high errors on steep slopes and often poorly represent ridges and valley bottoms (Gorokhovich and Voustianiouk 2006); Schwanghart and Scherler 2017~~; Gorokhovich and Voustianiouk 2006)~~. Coarser resolution also biases, or decreases the accuracy of, our estimates because DEM values along ridges are lowered by spatial averaging (Fujita et al. 2008). Both effects entail that modelled shadow outlines on glaciers increasingly lack detail and underestimate shadow length with coarser DEM resolution (Fig. 9~~7~~). Poor quality of the underlying DEM will propagate into estimates of glacier elevation change although trends derived from different DEMs are surprisingly consistent (Fig. 7). Satellite imagery obtained for the date of DEM acquisition can help quantify and correct for such biases.

Besides differences in resolution, the type of DEM also impacts the precision and accuracy of modelled shadows. Our analysis shows that among the DEMs with global coverage, the new GLO-30 DEM has the highest precision of derived shadows when compared to the benchmark swissALTI3D DEM, which is consistent with recent DEM assessments that underscore the high performance of the GLO-30 DEM (Guth and Geoffroy 2021) (Fig. 9~~7~~). Shadow outlines calculated from NASADEM and SRTM-1 are similar as they are obtained from the same data. We acknowledge that our method leaves any effects of SAR penetration into the snow pack atop the glacier ice ~~uncorrected~~ (Berthier et al. 2006). Yet, this offset can be treated as a constant when drawing bearing lines through shadows, given that the input DEM (SRTM) remains unchanged in our analysis. Snow cover can be thick in accumulation areas and may lead to biases (underestimates) when calculating glacier volume changes from DEM differencing (Gardelle et al. 2012). Though most shadows in our cases are in the ablation zone, we recommend to account for differing penetration depth in future studies that also include shadows on glaciers at very high elevations. The relatively low performance of the AW3D30 DEM in comparison to other global DEMs likely relates to hillslope and ridge artifacts caused by errors in optical DEM generation (Purinton and Bookhagen 2017). In any case, our Bayesian framework objectively propagates these errors and uncertainties. One promising avenue for future research is to use narrower priors based on previous research on glacier elevation change (Hugonnet et al. 2021) to further reduce uncertainty in the trends on glacier elevation changes.

In addition to the resolution and quality of the DEM, we expect that higher image resolution will warrant a higher accuracy and precision at which elevation changes can be detected (Fig. 7). We refrained from analyzing the effects of image resolution because we used only Landsat imagery with the longest freely available time series of satellite imagery. However, we recall that our trigonometric approach hinges on sun elevation and image resolution provided in the image meta data, both setting the detection limit of elevation changes. For example, for a sun elevation of 20° and a spatial resolution of 30 m, a minimum elevation change of 10.9 m can be detected unless subpixel classification approaches or pan-sharpening techniques are adopted (Liu and Wu 2005). Sun angle will be critical for our method (Rada Giacaman 2022) and we expect that our approach works better for images acquired during the winter months of the respective hemispheres as well as at higher latitudes. To determine interannual trends, we recommend using satellite imagery with similar time stamps within a year, given that glacier elevations are prone to seasonal variations (Moholdt et al. 2010).

Atmospheric refraction – the bending of solar light as it traverses the atmosphere – ~~leads to~~ causes an apparently higher sun elevation. The offset between the actual and apparent solar-position leads to errors in shadow-height applications depending mainly on solar elevation and, to a minor degree, on atmospheric pressure, humidity and temperature (Rada Giacaman 2022). Sun elevations in our study range between 15 and 40° which yields height difference errors of 0-2% (see Fig. 10 in Rada Giacaman, 2022). Additional error sources include uncertainties in the position of the satellite as well as problems in image registration and deformation. Yet, we did not account for errors due to atmospheric refraction and image registration as they appear minor compared to those related to image resolution and DEM quality.

Our study reveals and confirms decadal-scale loss of glacier mass. These changes are~~, which is~~ consistent with independent estimates of glacier elevation changes based on stereo-photogrammetric analysis~~the data~~ of US benchmark glaciers, i.er., South Cascade, Gulkana and Sperry Glacier (McNeil et al. (2022), and historic topographic maps of the Great Aletsch Glacier (Fischer et al. 2015; Leinss and Bernhard 2021). For the Baltoro Glacier, we detect no credible trends and independent, field-based validation data of surface changes at the shadow location are lacking. Yet, comparison of photographs from 1909 and 2004 show that glacier elevation changes at Concordia were low in the 20th century (<40 m) (Mayer et al. 2006). These small rates of surface lowering have been attributed to increases in precipitation and a lowering of summer mean and minimum temperatures in the Karakoram, supporting regionally unchanged glacier masses referred to as 'Karakoram Anomaly' (Hewitt 2005; Kääb et al. 2015; Forsythe et al. 2017; Farinotti et al. 2020).

We stress that our results are tied to local changes of shadows casted from adjacent mountains. Thus, we caution againstshould not be comparinged our results directly with glacier-wide mass balances because these integrate over entire glaciers or elevation bands within glaciers, and may refer to different study periods. whereas our results are representative for the shaded area only.For example, Hugonnet et al. (2021) estimate that the entire areas of Great Aletsch and South Cascade Glacier had elevation changes of -1.42 ± 0.1 and -0.66 ± 0.15 m yr^{-1} (mean and 1σ error), respectively, in 2000-2019. Our estimates are lower ($-1.08^{+0.056}/_{-0.05}$ and $-0.5742^{+0.171}/_{-0.171}$ m yr^{-1}, respectively) in the longer Landsat period, either because we measure elevation changes at higher parts of the glacier with possibly lower melt rates, or because glacier melt has accelerated in recent decadesyears (Hugonnet et al. 2021).- Elevation-dependent glacier melt could at least partly explain the higher melt rates in the lower-lying shadow of the Gulkana glacier (Gulkana West), although the high difference by a factor of 10 requires further analysis. We thus envision that our method could enhance, complement, and amend geodetic surveys in ablation and accumulation areas (Beedle et al. 2014). Potentially, ourOur method can be applied globally, but is restricted to those glaciers that are surrounded by steep stable topography. Our method becomes unsuccessful when the shadow edge constantly falls onto bedrock due to progressive glacier retreat –– a situation that will soon occur at the dwindling Sperry Glacier. Ideal environments for our approach are glaciers close to steep topography in high latitudes, producing sufficiently long cast shadows long enough to infer differences in bearing lines. Suitable sites remain to be identified and should, at best, have high-resolution DEMs with high precision and accuracy available. Locations with large landslides that lower mountain peaks (Shugar et al. 2021) should be avoided as they may violate the assumption of unaltered ridge topography over time. The processing steps developed in this study can be fully automated although quality control of the obtained geodetic bearing lines connecting modelled and actual shadow outlines are crucial.

5 Conclusions and outlook

In summary, our analysiswe shows that cast shadows offer avenues to retrieve ice-topographicglacier elevation changes from satellite imagery over many decades. We demonstrate for four glaciersselect cases that our method provides quantitative information about local the changes in glacier thickness elevation over with time. These changes that are consistent with independent DEMs of difference in ~~shadow-covered~~shaded areas. Accurately resolving glacier elevation changes hinges on t~~T~~he spatial resolution of the satellite imagery from which we mapped shadows~~ are retrieved~~, as well as the quality and resolution of the underlying DEM~~ DEMs is critical to the precision at which ice-topographic changes can be resolved~~. Upon the emergence of global, void-free, high-resolution satellite images and DEMs~~ with high precision~~, our method can be extended to historical satellite and aerial imagery, assuming~~ under the assumption~~ that the geometry of mountain ridges and peaks ~~has not changed significantly by earth surface processes~~remains unchanged with time. We conclude that our approach has the potential to complement existing or future ~~in~~ in-situ measuring networks anywhere on Earth where mountains shade parts of adjacent glaciers. We thus enrich glaciological and geodetic ~~assessment~~toolbox with a new method that helps quantifying glacier elevation ~~, providing data on ice-topographic~~ changes especially at high altitudes ~~for regions~~ with limited access.

Appendix A: Additional tables

Table A1: Landsat bands used to map shadows on glaciers, including image metadata, the threshold to manually classify shadows on glaciers, and the number of ~~geodetic~~ bearing lines that cross shadows on glaciers. TM: Thematic Mapper, ETM+: Enhanced Thematic Mapper, OLI: Operational Land Imager, SRTM-1: DEM of the Shuttle Radar Topography Mission (30m resolution), swissALTI3D: DEM of Switzerland (5 m resolution), GLO-90: Copernicus DEM (90m resolution)

Glacier	Acquisition Date	Landsat Mission	Band	Azimuth	Elevation	File Name in GeoTIFF format	Threshold between shadow and no-shadow	Number of ~~geodetic~~ bearing lines drawn
Great Aletsch	06.02.1987	TM	2	146.96~~4584~~	21.95~~4781~~	LT05_L1TP_195028_19870206_20170213_01_T1_sr_band2	5,500	106 (SRTM-1, swissALTI3D), 107 (GLO-90)
Great Aletsch	18.02.1988	TM	2	147.~~489700~~49	26.38~~2202~~	LT05_L1TP_194028_19880218_20180215_01_T1_sr_band2	5,500	106 (SRTM-1), 105 (GLO-90, swissALTI3D)
Great Aletsch	11.02.1989	TM	2	148.32~~4875~~	25.39~~4554~~	LT05_L1TP_195028_19890211_20180215_01_T1_sr_band2	5,500	105 (SRTM-1), 106 (GLO-90)
Great Aletsch	07.02.1990	TM	2	146.~~875916~~88	22.34~~4643~~	LT05_L1TP_194028_19900207_20180219_01_T1_sr_band2	5,500	105 (SRTM-1, swissALTI3D), 106 (GLO-90)
Great Aletsch	01.02.1991	TM	2	147.64~~2700~~	20.64~~2624~~	LT05_L1TP_195028_19910201_20180215_01_T2_sr_band2	5,500	106~~1~~ (SRTM-1, swissALTI3D), 105 (GLO-90)
Great Aletsch	06.02.1993	TM	2	147.11~~3144~~	22.21~~0066~~	LT05_L1TP_195028_19930206_20180215_01_T1_sr_band2	5,500	106 (SRTM-1), 105 (GLO-90, swissALTI3D)
Great Aletsch	25.02.1994	TM	2	144.21~~4462~~	28.10~~0639~~	LT05_L1TP_195028_19940225_20180215_01_T1_sr_band2	5,500	100 (SRTM-1), 101 (GLO-90, swissALTI3D)
Great Aletsch	21.02.1995	TM	2	142.~~355377~~356	25.~~59594~~60	LT05_L1TP_194028_19950221_20180215_01_T1_sr_band2	5,500	102 (SRTM-1, swissALTI3D), 101 (GLO-90, swissALTI3D)
Great Aletsch	21.02.1996	TM	2	142.07~~4844~~	23.06~~4941~~	LT05_L1TP_195028_19960215_20180215_01_T1_sr_band2	5,500	102 (SRTM-1, GLO-90, swissALTI3D)
Great Aletsch	01.02.1997	TM	2	148.~~578949~~58	21.19~~2062~~	LT05_L1TP_195028_19970201_20180215_01_T1_sr_band2	5,500	108 (SRTM-1), 107 (GLO-90, swissALTI3D)
Great Aletsch	20.02.1998	TM	2	148.~~899734~~90	27.~~876671~~88	LT05_L1TP_195028_19980220_20180215_01_T1_sr_band2	5,500	105 (SRTM-1, swissALTI3D), 106 (GLO-90)
Great Aletsch	10.02.2000	TM	2	149.53~~0487~~	24.~~195702~~20	LT05_L1TP_195028_20000210_20171211_01_T1_sr_band2	5,500	106 (SRTM-1, GLO-90, swissALTI3D)
Great Aletsch	14.02.2004	TM	2	150.~~348663~~35	25.~~929115~~93	LT05_L1TP_194028_20040214_20180311_01_T1_sr_band2	5,500	107 (SRTM-1), 106 (GLO-90), 108 (swissALTI3D)
Great Aletsch	07.02.2005	TM	2	153.~~.035782~~04	24.~~646736~~65	LT05_L1TP_195028_20050207_20180130_01_T1_sr_band2	5,500	107 (SRTM-1), 108 (GLO-90), 109 (swissALTI3D)
Great Aletsch	10.02.2006	TM	2	153.75~~2365~~	25.81~~0577~~	LT05_L1TP_195028_20060210_20180311_01_T1_sr_band2	5,500	107 (SRTM-1), 109 (GLO-90, swissALTI3D)
Great Aletsch	22.02.2007	TM	2	153.49~~3362~~	29.98~~2136~~	LT05_L1TP_194028_20070222_20180118_01_T1_sr_band2	5,500	106 (SRTM-1, GLO-90), 107 (swissALTI3D)

Great Aletsch	18.02.2009	TM	2	151.65~~1184~~	28.13~~4636~~	LT05_L1TP_195028_20090218_20180302_01_T2_sr_band2	5,500	109 (SRTM-1, swissALTI3D), 108 (GLO-90)
Great Aletsch	21.02.2010	TM	2	152.59~~1125~~	29.46~~365~~	LT05_L1TP_195028_20100221_20161016_01_T1_sr_band2	5,500	108 (SRTM-1, swissALTI3D), 106 (GLO-90)
Great Aletsch	08.02.2011	TM	2	153.~~846497~~85	25.~~078377~~08	LT05_L1TP_195028_20110208_20161010_01_T1_sr_band2	5,500	109 (SRTM-1, GLO-90, swissALTI3D)
Great Aletsch	25.02.2014	OLI	3	154.88~~1790~~	31.67~~6713~~	LC08_L1TP_194028_20140225_20170425_01_T1_sr_band3	5,500	108 (SRTM-1, swissALTI3D), 107 (GLO-90)
Great Aletsch	19.02.2015	OLI	3	155.~~215179~~22	29.~~37574~~38	LC08_L1TP_195028_20150219_20170412_01_T1_sr_band3	5,500	107 (SRTM-1), 108 (GLO-90), 110 (swissALTI3D)
Great Aletsch	15.02.2016	OLI	3	155.68~~3655~~	27.95~~2034~~	LC08_L1TP_194028_20160215_20170329_01_T1_sr_band3	5,500	110 (SRTM-1), 109 (GLO-90), 111 (swissALTI3D)
Great Aletsch	20.02.2018	OLI	3	165,56	21,33	LC08_L1TP_194028_20180220_20180308_01_T1	5,500	92 (GLO-90)
Great Aletsch	22.02.2019	OLI	3	155.~~717209~~72	27.70~~2271~~	LC08_L1TP_195028_20190214_20190222_01_T1_sr_band3	5,500	113 (SRTM-1), 109 (GLO-90), 112 (swissALTI3D)
Baltoro	11.02.1992	TM	3	141.60~~3058~~	30.55~~4222~~	LT05_L1TP_148035_19920211_20170123_01_T1_sr_band2	5,500	~~49 when only using SRTM / 50~~ 42 ~~when using SRTM and VFP~~
Baltoro	22.02.1996	TM	3	135.05~~2658~~	31.~~428848~~43	LT05_L1TP_148035_19960222_20170105_01_T1_sr_band2	5,000	~~40 / 42~~38
Baltoro	24.01.2000	ETM+	2	151.~~93563529~~94	29.~~47668300~~48	LE07_L1TP_148035_20000124_20170213_01_T1_B2	200	~~57 / 58~~31
Baltoro	15.02.2011	TM	2	147.~~356308~~36	34.91~~3021~~	LT05_L1TP_148035_20110215_20161010_01_T1_sr_band2	5,000	~~35 /~~ 30~~8~~
Baltoro	10.02.2015	OLI	3	150.~~857864~~86	34.~~447273~~45	LC08_L1TP_148035_20150210_20170413_01_T1_sr_band3	4,500	~~38 /~~ 2~~3~~9
Baltoro	29.02.2016	OLI	3	147.~~819061~~82	40.~~665691~~67	LC08_L1TP_148035_20160229_20170329_01_T1_sr_band3	5,000	~~26 / 30~~16
Baltoro	02.02.2018	OLI	3	152.16~~0034~~	32.33~~3149~~	LC08_L1TP_148035_20180202_20180220_01_T1_sr_band3	5,000	~~40 / 40~~29
Baltoro	08.02.2020	OLI	3	151.29~~0161~~	33.83~~334~~	LC08_L1TP_148035_20200208_20200211_01_T1_sr_band3	5,000	~~40 / 40~~28
Gulkana	13.03.1986	TM	2	157.84	21.25	LT05_L2SP_068015_19860313_20200917_02_T1	3,300 (West) / 2,700 (East)	42 (West) / 21 (East)
Gulkana	30.03.1989	TM	2	157.45	29.41	LT05_L2SP_067016_19890330_20200917_02_T1	3,300 / 3,000	20 / 10
Gulkana	19.03.1999	TM	2	160.07	25.25	LT05_L2SP_066016_19990319_20200908_02_T1	3,900 / 3,800	21 / 8
Gulkana	14.03.2009	TM	2	162.21~~4737~~	23.80~~0697~~	LT05_L1TP_066016_20090314_20160906_01_T1_sr_band2	5,500	22 / 8~~179~~
Gulkana	04.03.2011	TM	2	162.93	19.74	LT05_L2SP_066016_20110304_20200823_02_T1	2,900 / 2,700	24 / 22

Gulkana	06.03.2014	OLI	3	165.732956	17.113144	LC08_L1TP_066016_20140224_20170306_01_T1_sr_band3	6,500	23 / 23210
Gulkana	27.02.2015	OLI	3	165.491165	18.1244138	LC08_L1TP_066016_20150227_20170227_01_T1_sr_band3	7,500	25 / 210
Gulkana	21.02.2016	OLI	3	165.59820660	15.8144644	LC08_L1TP_067016_20160221_20170224_01_T1_sr_band3	7,000	25 / 23189
Gulkana	02.03.2017	OLI	3	165.54	19.48	LC08_L2SP_068016_20170302_20200905_02_T1	3,650 / 3,000	24 / 23
Gulkana	07.03.2018	OLI	3	165.56	21.33	LC08_L2SP_066016_20180307_20200901_02_T1	4,000 / 3,500	25 / 20
Gulkana	22.02.2019	OLI	3	165.5400833	16.271332	LC08_L1TP_066016_20190222_20190308_01_T1_sr_band3	5,500	25 / 22215
Gulkana	16.02.2020 and 25.02.2020	OLI	3	165.56791757	17.29818730	LC08_L1TP_066016_20200225_20200313_01_T1_sr_band3	6,000	52 / 47214
Gulkana	06.03.2021	OLI	3	165.62	21.05	LC08_L2SP_067016_20210306_20210317_02_T1	4,400 / 3,000	25 / 23
South Cascade	02.02.1987	TM	2	148.871033	18.9089505	LT05_L1TP_046026_19870202_20161003_01_T1_sr_band2	5,000	34
South Cascade	18.02.1993	TM	2	147.044220	23.97637998	LT05_L1TP_046026_19930218_20160928_01_T1_sr_band2	5,000	32
South Cascade	05.02.1994	TM	2	148.492279	19.78564579	LT05_L1TP_046026_19940205_20160927_01_T1_sr_band2	5,000	334
South Cascade	11.02.1996	TM	2	144.092560	20.011215	LT05_L1TP_046026_19960211_20160925_01_T1_sr_band2	5,000	29
South Cascade	22.02.1997	TM	2	147.531799	25.733513	LT05_L1TP_045026_19970222_20160924_01_T1_sr_band2	5,000	31
South Cascade	29.01.2000	ETM+	2	157.09748699100	20.21436407	LE07_L1TP_046026_20000129_20161003_01_T1_B2	100	32
South Cascade	20.02.2002	TM	2	150.9766492	25.97904298	LT05_L1TP_045026_20020220_20160916_01_T1_sr_band2	5,000	32
South Cascade	07.02.2003	TM	2	151.1876193	21.31980132	LT05_L1TP_045026_20030207_20160916_01_T2_sr_band2	5,000	33
South Cascade	10.02.2004	TM	2	152.290070	22.594368	LT05_L1TP_045026_20040210_20160914_01_T2_sr_band2	5,000	33
South Cascade	15.02.2006	TM	2	154.723404	25.24560525	LT05_L1TP_045026_20060215_20160911_01_T1_sr_band2	5,000	29
South Cascade	02.02.2007	TM	2	157.053238	21.43829344	LT05_L1TP_045026_20070202_20160911_01_T1_sr_band2	5,000	31
South Cascade	07.02.2009	TM	2	154.3108121	22.45902346	LT05_L1TP_045026_20090207_20160906_01_T1_sr_band2	5,000	32
South Cascade	17.02.2010	TM	2	154.5657983	25.933197	LT05_L1TP_046026_20100217_20160904_01_T1_sr_band2	5,000	32
South Cascade	20.02.2011	TM	2	154.06622307	26.81730782	LT05_L1TP_046026_20110220_20160901_01_T1_sr_band2	5,000	33

South Cascade	15.02.2015	OLI	3	157.~~108383~~11	25.~~78627~~79	LC08_L1TP_046026_20150215_20170301_01_T1_sr_band3	5,000	28
South Cascade	13.02.2017	OLI	3	157.~~278580~~28	25.30~~0629~~	LC08_L1TP_045026_20170213_20180201_01_T2_sr_band3	5,000	31
Sperry	28.02.1986	TM	2	147.03~~1769~~	27.79~~0085~~	LT05_L1TP_041026_19860228_20161004_01_T1_sr_band2	3,500	~~33~~25
Sperry	19.02.2000	TM	2	149.8~~7~~8~~403~~	25.~~038727~~04	LT05_L1TP_041026_20000219_20160918_01_T1_sr_band2	3,500	~~23~~11
Sperry	27.02.2003	TM	2	149.10~~99426~~	28.04~~4254~~	LT05_L1TP_041026_20030227_20160916_01_T1_sr_band2	3,500	~~33~~27
Sperry	19.02.2006	TM	2	154.37~~2833~~	26.61~~2225~~	LT05_L1TP_041026_20060219_20160911_01_T1_sr_band2	3,500	~~34~~12
Sperry	25.02.2008	TM	2	153.74~~2905~~	28.~~536865~~54	LT05_L1TP_041026_20080225_20160906_01_T1_sr_band2	3,500	~~30~~12
Sperry	25.02.2014	OLI	3	156.~~529221~~53	29.~~456596~~46	LC08_L1TP_041026_20140225_20170307_01_T1_sr_band3	3,500	~~33~~17
Sperry	28.02.2015	OLI	3	156.08~~1711~~	30.42~~4019~~	LC08_L1TP_041026_20150228_20170301_01_T1_sr_band3	3,500	~~33~~20

Table A2: DEMs used to simulate shadows on glaciers, including spatial resolution, acquisition date, and data source.

DEM	Investigated Glacier	Spatial resolution [m]	Acquisition date	Source
swissALTI3D	Great Aletsch	(downsampled to 5m)	2017-2018	https://www.swisstopo.admin.ch/en/geodata/height/alti3d.html
Viewfinder Panoramas	Baltoro	~90 (3-Arc seconds)30 m	diverse	http://viewfinderpanoramas.org/
ArcticDEM	Gulkana	2	2009	https://www.pgc.umn.edu/data/arcticdem/ SETSM_WV01_20090616_10200100079A2600_1020010007D06000_seg1_2m_v3.0.tif (used item: SETSM_~1.TIF)
SRTM-1	Great Aletsch, Baltoro, Gulkana, South Cascade, Sperry	~30 (1-Arc second)	2000	http://www.opentopography.org
SRTM-3	Great Aletsch	~90 (3-Arc seconds)	2000	http://www.opentopography.org
NASADEM	Great Aletsch	30	2000	http://www.opentopography.org
ALOS World 3D World (AW3D30)	Great Aletsch	30	2006-2011	http://www.opentopography.org
Copernicus Global DEM (GLO-30)	Great Aletsch	30	20110-2015	http://www.opentopography.org
Copernicus Global DEM (GLO-90)	Great Aletsch	90	20110-2015	http://www.opentopography.org

Table A3: Prior and posterior distributions of the parameters in the hierarchical ~~local~~ models of glacier elevation change Δh with year y using ~~geodetic~~ bearing lines (Eqs. 1-11).

Parameter	Prior	Posterior Median | 2.5% | 97.5% of HDI
α	Normal (mean = 0, sd = 2.5)	0.23~~06~~ | -0.14 ~~08~~| 0.6~~2~~1
β	Normal (mean = 0, sd = 2.5)	-0.31~~2~~ | -0.64~~88~~ | 0.03~~25~~
σ_α	Normal (mean = 0, sd = 2.5) T(0,)	0.4~~1~~3 | 0.22~~04~~ | 0.90~~37~~
σ_β	Normal (mean = 0, sd = 2.5) T(0,)	0.38~~54~~ | 0.19~~22~~ | 0.80~~1.39~~
κ	Normal (mean = 0, sd = 2.5) T(0,)	0.55~~2~~ | 0.53~~1~~ | 0.57~~4~~
ς	LKJ~~kj~~Cholesky(1) on **R**	0.74~~35~~ | -0.00~~69~~ | 0.98~~6~~

Notes: Priors refer to standardised input data pairs of Δh and y using a mean of zero and unit standard deviation. T(-·, ·) indicates a truncation of the distribution at a~~n~~ lower or upper boundary. sd, standard deviation. Degrees of freedom are constant (ν = 3) and have no posterior estimate.

Table A4: Prior and posterior distributions of the parameters in the ~~local~~ hierarchial models of glacier elevation change Δh with year y using all data (within and outside the Landsat period) and only for data within the Landsat period, determined from ~~from~~ reference DEMs and historical maps (Eqs. 1-11).

Parameter	Prior	Posterior for all available data Median | 2.5% | 97.5% of HDI	Posterior for data from the Landsat era only Median | 2.5% | 97.5% of HDI
α	Normal (mean = 0, sd = 2.5)	0.17~~8~~ | -0.85 ~~1.05~~| 1.16~~42~~	0.17~~22~~ | -0.99~~1.14~~| 1.32~~56~~
β	Normal (mean = 0, sd = 2.5)	-0.48~~55~~ | -1.02~~25~~ | 0.06~~18~~	-0.32~~43~~ | -0.64~~99~~ | 0.04~~23~~
σ_α	Normal (mean = 0, sd = 2.5) T(0,)	1.03~~12~~ | 0.45~~2~~ | 2.42~~85~~	1.19~~27~~ | 0.52~~48~~ | 2.69~~3.13~~
σ_β	Normal (mean = 0, sd = 2.5) T(0,)	0.52~~6~~ | 0.45~~17~~ | 2.42~~1.81~~	0.27~~36~~ | -0.01 | 0.8~~1.5~~8
κ	Normal (mean = 0, sd = 2.5) T(0,)	0.26~~7~~ | 0.18~~8~~ | 0.37~~4~~	0.21~~4~~ | 0.12 | 0.34~~45~~
ς	LkjCholesky(1) on **R**	0.44~~37~~ | -0.55~~68~~ | 0.97	~~-~~0.01~~7~~ | -0.87~~94~~ | 0.88~~92~~

Notes: Priors refer to standardised input data pairs of Δh and y using a mean of zero and unit standard deviation. T(·, ·) indicates a truncation of the distribution at a~~n~~ lower or upper boundary. sd, standard deviation. Degrees of freedom are constant (ν = 3) and have no posterior estimate.

Table A5: Comparison of heights at stable terrain (ST) in Landeskarte over time and with different DEMS.

year	ST1	ST2	ST3	ST4	ST5	ST6	ST7	ST8	ST9	ST10
1959	3465	3366	3242,6	4195	3810,7	3754	3641 (snow)	2994,8	2951,7	3016,2
1968	3466	3366	3242,6	4195	3810,7	3754	3641 (snow)	2994,8	2951,7	3016,2
1971	3466	3366	3242,6	4195	3810,7	3754	3641 (snow)	2994,8	2951,7	3016,2
1975	3466	3366	3242,6	4195	3810,7	3754	3641 (snow)	2994,8	2951,7	3016,2
1981	3463	3366	3242,6	4195	3810,7	3754	3639	2994,8	2951,8	3016,2
1987	3463	3366	3242,6	4195	3810,7	3754	3639	2994,8	2951,8	3016,2
1993	3463	3366	3242,6	4193	3810,7	3754	3639	2995	2952	3016
1999	3463	3366	3242,6	4193	3810,7	3754	3639	2995	2952	3016
2005	3463	3366	3242,6	4193	3810,7	3754	3639	2995	2952	3016
2011	3463	3366	3243	4193	3811	3754	3639	2995	2952	3016
2016	3463	3366	3243	4193	3811	3754	3639	2995	2952	3016
2020	3463	3366	3243	4194	3811	3756	3639	2995	2952	3016
swissALTI3D	3460,5	3364,4	3242,2	NA	3810,2	3754,95	3638,1	2995,98	2953,1	3020,9
Cop90	3386,9	3277,9	3114,9	4133,2	3750,2	3694,3	3571,2	2858,1	2894,5	2956,98
Cop30	3389,9	3314,8	3119,6	4144,4	3791,7	3702,8	3584,9	2903,5	2926,2	3003,4

Figure A1: Webpage with historical maps (Landeskarte) from the Bundesamt für Landestopografie KOGIS (Koordination, Geoinformation und Services, https://www.swisstopo.admin.ch)

Notes: Red circles (ST1-ST10) represent locations of stable terrains (ST) that were investigated and compared with heights in different DEMs to proof the quality of the historical maps. Red dots represent locations we used to validate our results of glacier elevation changes.

Data and code availability

The outlines of the shadows, the ~~geodetic~~ bearing lines, tables with inferred elevation changes for each glacier, and the Bayesian multi-level models are available via *Zenodo* (https://doi.org/10.5281/zenodo.7799940~~10.5281/zenodo.7134743~~). Landsat images were obtained from *EarthExplorer* (https://usgs.earthexplorer.gov), and all DEMs from which we derived shadows are freely available from the sources provided in Table A2. DEMs for validation are available at https://alaska.usgs.gov/products/data/glaciers/benchmark_geodetic.php.

Codes to fit the Bayesian multi-level models are available at *GitHub* (https://github.com/geveh/ShadowsOnGlaciers).

Author contributions

All authors contributed equally in designing the study, conducting the analysis, validating the results, and writing the manuscript.

Competing interests

The authors declare that they have no conflict of interest.

Acknowledgements

~~The authors thank~~We are indebted to the hep from Romain Hugonnet who~~for~~ provided~~ing~~ data on ~~glacier~~ elevation changes within shaded glacier surfaces~~ows~~.~~the German Academic Exchange Service (DAAD) for their funding of Co-PREPARE.~~

Financial support

MP was supported for one year by a stipend by the German Academic Exchange Service (DAAD) within the ~~DAAD-funded~~ project Co-PREPARE, a collaborati~~on~~~~ve project~~ between the University of Potsdam and the Indian Institute of Technology Roorkee.

References

Azam, M. F.; Kargel, J. S.; Shea, J. M.; Nepal, S.; Haritashya, U. K.; Srivastava, S.; Maussion, F.; Qazi, N.; Chevallier, P.; Dimri, A. P.; Kulkarni, A. V.; Cogley, J. G.; and Bahuguna, I.~~ et al.~~: Glaciohydrology of the Himalaya-Karakoram, *Science (New York, N.Y.)* 373 (6557), doi: 10.1126/science.abf3668, 2021.

Bauder, A.; Funk, M.; and Huss, M.: Ice-volume changes of selected glaciers in the Swiss Alps since the end of the 19th century, *Ann. Glaciol.* 46, pp. 145–149, doi: 10.3189/172756407782871701, 2007.

Beedle, M. J.; Menounos, B.; and Wheate, R.: An evaluation of mass-balance methods applied to Castle creek Glacier, British Columbia, Canada, *J. Glaciol.* 60 (220), pp. 262–276, doi: 10.3189/2014JoG13J091, 2014.

Belart, J. M. C.; Magnússon, E.; Berthier, E.; Gunnlaugsson, Á. Þ.; Pálsson, F.; Aðalgeirsdóttir, G.; Jóhannesson, T.; Thorsteinsson, T.; and Björnsson, H.: Mass Balance of 14 Icelandic Glaciers, 1945–2017: Spatial Variations and Links With Climate, *Front. Earth Sci.* 8, Article 163, doi: 10.3389/feart.2020.00163, 2020.

Berthier, E.; Arnaud, Y.; Vincent, C.; and Rémy, F.: Biases of SRTM in high-mountain areas: Implications for the monitoring of glacier volume changes, *Geophys. Res. Lett.* 33 (8), doi: 10.1029/2006GL025862, 2006.

Bolch, T.; Pieczonka, T.; and Benn, D. I.: Multi-decadal mass loss of glaciers in the Everest area (Nepal Himalaya) derived from stereo imagery, *The Cryosphere* 5 (2), pp. 349–358, doi: 10.5194/tc-5-349-2011, 2011.

Brighenti, S.; Tolotti, M.; Bruno, M. C.; Wharton, G.; Pusch, M. T.; and Bertoldi, W.: Ecosystem shifts in Alpine streams under glacier retreat and rock glacier thaw: A review, *The Science of the total environment* 675, pp. 542–559, doi: 10.1016/j.scitotenv.2019.04.221, 2019.

Bürkner, P. C.: brms: An R Package for Bayesian Multilevel Models Using Stan, *J. Stat. Soft.* 80 (1), doi: 10.18637/jss.v080.i01, 2017.

Cauvy-Fraunié, S.~~;~~ and Dangles, O.: A global synthesis of biodiversity responses to glacier retreat, *Nature ecology & evolution* 3 (12), pp. 1675–1685, doi: 10.1038/s41559-019-1042-8, 2019.

Conrad, O.; Bechtel, B.; Bock, M.; Dietrich, H.; Fischer, E.; Gerlitz, L.; Wehberg, J.; Wichmann, V.; and Böhner, J.~~et al.~~: System for Automated Geoscientific Analyses (SAGA) version 2.1.4, *Geosci. Model Dev.* 8 (7), pp. 1991–2007, doi: 10.5194/gmd-8-1991-2015, 2015.

De Ferranti, J.: Digital Elevation Data: SRTM Void Fill. Viewfinder Panoramas, available online at *http://www.viewfinderpanoramas.org/voidfill.html*, updated on 12/21/2015, checked on 8/28/2022, 2015.

Dematteis, N.; Giordan, D.; Crippa, B.; and Monserrat, O.: Measuring Glacier Elevation Change by Tracking Shadows on Satellite Monoscopic Optical Images, *IEEE Geosci. Remote Sensing Lett.* 20, pp. 1–5, doi: 10.1109/LGRS.2022.3231659, 2023.

EROS (Earth Resources Observation And Science) Center: USGS EROS Archive – Digital Elevation – Shuttle Radar Topography Mission (SRTM) Non-Void Filled, available online at *https://www.usgs.gov/centers/eros/science/usgs-eros-archive-digital-elevation-shuttle-radar-topography-mission-srtm-non*, checked on 28/3/2023, 2018.

Farías-Barahona, D.; Sommer, C.; Sauter, T.; Bannister, D.; Seehaus, T. C.; Malz, P.; Casassa, G.; Mayewski, P. A.; Turton, J. V.; and Braun, M. H.~~et al.~~: Detailed quantification of glacier elevation and mass changes in South Georgie, *Environ. Res. Lett.* 15 (3), p. 34036, doi: 10.1088/1748-9326/ab6b32, 2020.

Farinotti, D.; Huss, M.; Fürst, J. J.; Landmann, J.; Machguth, H.; Maussion, F.; and Pandit, A.: A consensus estimate for the ice thickness distribution of all glaciers on Earth, *Nat. Geosci.* 12 (3), pp. 168–173, doi: 10.1038/s41561-019-0300-3, 2019.

Farinotti, D.; Immerzeel, W. W.; De Kok, R.; Quincey, D. J.; and Dehecq, A.: Manifestations and mechanisms of the Karakoram glacier Anomaly, *Nature geoscience* 13 (1), pp. 8–16, doi: 10.1038/s41561-019-0513-5, 2020.

Farr, T. G.; Rosen, P. A.; Caro, E.; Crippen, R.; Duren, R.; Hensley, S.; Kobrick, M.; Paller, M.; Rodriguez, E.; Roth, L.; Seal, D.; Shaffer, S.; Shimada, J.; Umland, J.; Werner, M.; Oskin, M.; Burbank, D.; and Alsdorf, D.~~et al.~~: The Shuttle Radar Topography Mission, *Rev. Geophys.* 45 (2), doi: 10.1029/2005RG000183, 2007.

Fischer, M.; Huss, M.; and Hoelzle, M.: Surface elevation and mass changes of all Swiss glaciers 1980–2010, *The Cryosphere* 9 (2), pp. 525–540, doi: 10.5194/tc-9-525-2015, 2015.

Forsythe, N.; Fowler, H. J.; Li, X. F.; Blenkinsop, S.; and Pritchard, D.: Karakoram temperature and glacial melt driven by regional atmospheric circulation variability, *Nature Clim Change* 7 (9), pp. 664–670, doi: 10.1038/nclimate3361, 2017.

Fujita, K.; Suzuki, R.; Nuimura, T.; and Sakai, A.: Performance of ASTER and SRTM DEMs, and their potential for assessing glacial lakes in the Lunana region, Bhutan Himalaya, *J. Glaciol.* 54 (185), pp. 220–228, doi: 10.3189/002214308784886162, 2008.

Gardelle, J.; Berthier, E.; and Arnaud, Y.: Impact of resolution and radar penetration on glacier elevation changes computed from DEM differencing, *J. Glaciol.* 58 (208), pp. 419–422, doi: 10.3189/2012JoG11J175, 2012.

Geyman, E. C.; van Pelt, W. J. J.; Maloof, A. C.; Aas, H. F.; and Kohler, J.: Historical glacier change on Svalbard predicts doubling of mass loss by 2100, *Nature* 601 (7893), pp. 374–379, doi: 10.1038/s41586-021-04314-4, 2022.

Gorokhovich, Y.~~;~~ and Voustianiouk, A.: Accuracy assessment of the processed SRTM-based elevation data by CGIAR using field data from USA and Thailand and its relation to the terrain characteristics, *Remote Sensing of Environment* 104 (4), pp. 409–415, doi: 10.1016/j.rse.2006.05.012, 2006.

Guth, P. L.~~;~~ and Geoffroy, T. M.: LiDAR point cloud and ICESat-2 evaluation of 1 second global digital elevation models: Copernicus wins, *Transactions in GIS* 25 (5), pp. 2245–2261, doi: 10.1111/tgis.12825, 2021.

Hewitt, K.: The Karakoram Anomaly? Glacier Expansion and the 'Elevation Effect,' Karakoram Himalaya, *Mountain Research and Development* 25 (4), pp. 332–340, doi: 10.1659/0276-4741(2005)025[0332:TKAGEA]2.0.CO;2, 2005.

Huggel, C.; Clague, J. J.; and Korup, O.: Is climate change responsible for changing landslide activity in high mountains?, *Earth Surf. Process. Landforms* 37 (1), pp. 77–91, doi: 10.1002/esp.2223, 2012.

Hugonnet, R.; McNabb, R.; Berthier, E.; Menounos, B.; Nuth, C.; Girod, L.; Farinotti, D.; Huss, M.; Dussaillant, I.; Brun, F.; and Kääb, A. ~~et al.~~: Accelerated global glacier mass loss in the early twenty-first century, *Nature* 592 (7856), pp. 726–731, doi: 10.1038/s41586-021-03436-z, 2021.

IPCC: Special Report on the Ocean and Cryosphere in a Changing Climate, edited by H.-O. Pörtner, D.C. Roberts, V. Masson-Delmotte, P. Zhai, M. Tignor, E. Poloczanska, K. Mintenbeck, A. Alegría, M. Nicolai, A. Okem, J. Petzold, B. Rama, N.M. Weyer, available online at *https://www.ipcc.ch/srocc/*, checked on 8/28/2022, 2019.

Kääb, A.; Treichler, D.; Nuth, C.; and Berthier, E.: Brief Communication: Contending estimates of 2003–2008 glacier mass balance over the Pamir–Karakoram–Himalaya, *The Cryosphere* 9 (2), pp. 557–564, doi: 10.5194/tc-9-557-2015, 2015.

Kääb, A.; Winsvold, S.; Altena, B.; Nuth, C.; Nagler, T.; and Wuite, J.: Glacier Remote Sensing Using Sentinel-2. Part I: Radiometric and Geometric Performance, and Application to Ice Velocity, *Remote Sensing* 8 (7), p. 598, doi: 10.3390/rs8070598, 2016.

Kruschke, J.: Doing Bayesian data analysis. A tutorial with R, JAGS, and Stan, 2nd ed.: Elsevier, 2014.

Leinss, S.~~;~~ and Bernhard, P.: TanDEM-X:Deriving InSAR Height Changes and Velocity Dynamics of Great Aletsch Glacier, *IEEE J. Sel. Top. Appl. Earth Observations Remote Sensing* 14, pp. 4798–4815, doi: 10.1109/JSTARS.2021.3078084, 2021.

Li, D.; Lu, X.; Overeem, I.; Walling, D. E.; Syvitski, J.; Kettner, A. J.; Bookhagen, B.; Zhou, Y.; and Zhang, T. ~~et al.~~: Exceptional increases in fluvial sediment fluxes in a warmer and wetter High Mountain Asia, *Science (New York, N.Y.)* 374 (6567), pp. 599–603, doi: 10.1126/science.abi9649, 2021.

Li, H.; Xu, L.; Shen, H.; and Zhang, L.: A general variational framework considering cast shadows for the topographic correction of remote sensing imagery, *ISPRS Journal of Photogrammetry and Remote Sensing* 117, pp. 161–171, doi: 10.1016/j.isprsjprs.2016.03.021, 2016.

Liu, K.; Song, C.; Ke, L.; Jiang, L.; Pan, Y.; and Ma, R.: Global open-access DEM performances in Earth's most rugged region High Mountain Asia: A multi-level assessment, *Geomorphology* 338, pp. 16–26, doi: 10.1016/j.geomorph.2019.04.012, 2019.

Liu, W.~~;~~ and Wu, E. Y.: Comparison of non-linear mixture models: sub-pixel classification, *Remote Sensing of Environment* 94 (2), pp. 145–154, doi: 10.1016/j.rse.2004.09.004, 2005.

Mannerfelt, E. S.; Dehecq, A.; Hugonnet, R.; Hodel, E.; Huss, M.; Bauder, A.; and Farinotti, D.: Halving of Swiss glacier volume since 1931 observed from terrestrial image photogrammetry, *The Cryosphere* 16 (8), pp. 3249–3268, doi: 10.5194/tc-16-3249-2022, 2022.

Mayer, C.; Lambrecht, A.; Belò, M.; Smiraglia, C.; and Diolaiuti, G.: Glaciological characteristics of the ablation zone of Baltoro glacier, Karakoram, Pakistan, *Ann.~~als of~~ Glaciol.~~ogy~~* 43, pp. 123–131, doi: 10.3189/172756406781812087, 2006.

McElreath, R.: Statistical Rethinking: Chapman and Hall/CRC, 2020.

McNeil, C. J.; Florentine, C. E.; Bright, V. A. L.; Fahey, M. J.; McCann, E.; Larsen, C. F.; Thomas, E. E.; Shean, D. E.; McKeon, L. A.; March, R. S.; Keller, W.; Whorton, E. N.; O'Neel, S.; Baker, E. H.; Sass, L., C.; and Bollen, K. E.~~ et al.~~: Geodetic Data for USGS Benchmark Glaciers: Orthophotos, Digital Elevation Models, Glacier Boundaries and Surveyed Positions, version 2.0, *US Geological Survey data release*, doi: 10.5066/P9R8BP3K, 2022.

Millan, R.; Mouginot, J.; Rabatel, A.; Morlighem, M.: Ice velocity and thickness of the world's glaciers, *Nature geoscience* 15 (2), pp. 124–129, doi: 10.1038/s41561-021-00885-z, 2022.

Milner, A. M.; Khamis, K.; Battin, T. J.; Brittain, J. E.; Barrand, N. E.; Füreder, L.; Cauvy-Fraunié, S.; Gíslason. G. M.; Jacobsen, D.; Hannah, D. M.; Hodson, A. J.; Hood, E.; Lencioni, V.; Ólafsson, J. S.; Robinson, C. T.; Traner, M.; and Brown, L. E.~~ et al.~~: Glacier shrinkage driving global changes in downstream systems, *Proceedings of the National Academy of Sciences of the United States of America* 114 (37), pp. 9770–9778, doi: 10.1073/pnas.1619807114, 2017.

Minora, U.; Senese, A.; Bocchiola, D.; Soncini, A.; D'agata, C.; Ambrosini, R.; Mayer, C.; Lambrecht, A.; Vuillermoz, E.; Smiraglia, C.; and Diolaitui, G.~~ et al.~~: A simple model to evaluate ice melt over the ablation area of glaciers in the Central Karakoram National Park, Pakistan, *Ann.~~als of~~ Glaciol.~~ogy~~* 56 (70), pp. 202–216, doi: 10.3189/2015AoG70A206, 2015.

Moholdt, G.; Nuth, C. Hagen, J. O.~~;~~ and Kohler, J.: Recent elevation changes of Svalbard glaciers derived from ICESat laser altimetry, *Remote Sensing of Environment* 114 (11), pp. 2756–2767, doi: 10.1016/j.rse.2010.06.008, 2010.

Mukul, M.; Srivastava, V.; Jade, S.; and Mukul, M.: Uncertainties in the Shuttle Radar Topography Mission (SRTM) Heights: Insights from the Indian Himalaya and Peninsula, *Scientific reports* 7, p. 41672, doi: 10.1038/srep41672, 2017.

Neckel, N.; Kropáček, J.; Bolch, T.; and Hochschild, V.: Glacier mass changes on the Tibetan Plateau 2003–2009 derived from ICESat laser altimetry measurements, *Environ. Res. Lett.* 9 (1), p. 14009, doi: 10.1088/1748-9326/9/1/014009, 2014.

Paul, F.; Andreassen, L. M.; and Winsvold, S. H.: A new glacier inventory for the Jostedalsbreen region, Norway, from Landsat TM scenes of 2006 and changes since 1966, *Ann. Glaciol.* 52 (59), pp. 153–162, doi: 10.3189/172756411799096169, 2011.

Paul, F.; Kääb, A.; Maisch, M.; Kellenberger, T.; and Haeberli, W., International Glaciological Society: The new remote-sensing-derived Swiss glacier inventory: I. Methods, *Ann.~~als of~~ Glaciol.~~ogy~~* (34), 355 - 361, 2002.

Paul, F.; Winsvold, S.; Kääb, A.; Nagler, T.; and Schwaizer, G.: Glacier Remote Sensing Using Sentinel-2. Part II: Mapping Glacier Extents and Surface Facies, and Comparison to Landsat 8, *Remote Sensing* 8 (7), p. 575, doi: 10.3390/rs8070575, 2016.

Pfeffer, W. T.~~ad~~; Arendt, A.~~nthony~~ A.; Bliss, A.~~ndrew~~; Bolch, T.~~obias~~; Cogley, J. G.~~raham~~; Gardner, A.~~lex~~ S.; Hagen, J. O.; Hock, R.; Kaser, G.; Kienholz, C.; Miles, E. S.; Moholdt, G.; Mölg, N.; Paul, F.; Radić, V.; Rastner, P.; Raup, B. H.; Rich, J.; Sharp, M. J.; and The Randolph Consortium~~ et al.~~: The Randolph Glacier Inventory: A globally complete inventory of glaciers, *J. Glaciol.* 60 (No. 221), pp. 537–552, doi: 10.3189/2014JoG13J176, 2014.

Pritchard, H. D.: Asia's shrinking glaciers protect large populations from drought stress, *Nature* 569 (7758), pp. 649–654, doi: 10.1038/s41586-019-1240-1, 2019.

Purinton, B.~~;~~ and Bookhagen, B.: Validation of digital elevation models (DEMs) and comparison of geomorphic metrics on the southern Central Andean Plateau, *Earth Surface Dynamics* 5 (2), pp. 211–237, doi: 10.5194/esurf-5-211-2017, 2017.

R Core Team: R: The R Project for Statistical Computing. Vienna, Austria, available online at *https://www.r-project.org/*, updated on 6/23/2022, checked on 8/17/2022, 2022.

Racoviteanu, A.~~;~~ and Williams, M. W.: Decision Tree and Texture Analysis for Mapping Debris-Covered Glaciers in the Kangchenjunga Area, Eastern Himalaya, *Remote Sensing* 4 (10), pp. 3078–3109, doi: 10.3390/rs4103078, 2012.

Rada Giacaman, C. A.: High-Precision Measurement of Height Differences from Shadows in Non-Stereo Imagery: New Methodology and Accuracy Assessment, *Remote Sensing* 14 (7), p. 1702, doi: 10.3390/rs14071702, 2022.

Rankl, M.~~;~~ and Braun, M.: Glacier elevation and mass changes over the central Karakoram region estimated from TanDEM-X and SRTM/X-SAR digital elevation models, *Ann. Glaciol.* 57 (71), pp. 273–281, doi: 10.3189/2016AoG71A024, 2016.

Richardson, S. D.~~;~~ and Reynolds, J. M.: An overview of glacial hazards in the Himalayas, *Quaternary International* 65-66, pp. 31–47, doi: 10.1016/S1040-6182(99)00035-X, 2000.

Richter, R.: Correction of satellite imagery over mountainous terrain, *Applied optics* 37 (18), pp. 4004–4015, doi: 10.1364/AO.37.004004, 1998.

Schwanghart, W.~~;~~ and Scherler, D.: Bumps in river profiles: uncertainty assessment and smoothing using quantile regression techniques, *Earth Surf. Dynam.* 5 (4), pp. 821–839, doi: 10.5194/esurf-5-821-2017, 2017.

Shugar, D. H.; Jacquemart, M.; Shean, D.; Bhushan, S.; Upadhyay, K.; Sattar, A.; Schwanghart, W.; MCBride, S.; Van Wyk de Vries, M.; Mergili, M.; Emmer, A.; Deschamps-Berger, C.; MCDonnell, M.; Bhambri, R.; Allen, S.; Berthier, E.; Carrivivk, J. L.; Clague, J. J.; Dokukin, M.; Dunning, S. A.; Frey, H.; Gascoin, S.; Haritashya, U. K.; Huggel, C.; Kääb, A.; Kargel, J. S.; Kavanaugh, J. L.; Lacroix, P.; Petley, D.; Pupper, S.; Azam, M. F.; Cook, S. J.; Dimri, A. P.; Eriksson, M.; Farinotti, D.; Fiddes, J.; Gnyawali, K. R.; Harrison, S.; Jha, M.; Koppes, M.; Kumar, A.; Leinss, S.; Majeed, U.; Mal, S.; Muhuri, A.; Noetzli, J.; Paul, F.; Rashid, I.; Sain, K.; Steiner, J.; Ugalde, F.; Watson, C. S.; and Westoby, M. J. ~~et al.~~: A massive rock and ice avalanche caused the 2021 disaster at Chamoli, Indian Himalaya, *Science (New York, N.Y.)* 373 (6552), pp. 300–306, doi: 10.1126/science.abh4455, 2021.

Stan Development Team: Stan Modeling Language Users Guide and Reference Manual, version 2.30, available online at *https://mc-stan.org/*, updated on 7/2/2022, checked on 8/17/2022, 2022.

Veh, G.; Korup, O.; and Walz, A.: Hazard from Himalayan glacier lake outburst floods, *Proceedings of the National Academy of Sciences of the United States of America* 117 (2), pp. 907–912, doi: 10.1073/pnas.1914898117, 2020.

Wulder, M. A.; Loveland, T. R.; Roy, D. P.; Crawford, C. J.; Masek, J. G.; Woodcock, C. E.; Allen, R. G.; Anderson, M. C.; Belward, A. S.; Cohen, W. B.; Dweyer, J.; Erb, A.; Gao, F.; Griffiths, P.; Helder, D.; Hermosilla, T.; Hipple, J. D.; Hostert, P.; Hughes, M. J.; Huntington, J.; Johnson, D., M.; Kennedy, R.; Kilic, A.; Li, Z.; Lymburner, L.; McCorkel, J.; Pahlevan, N.; Scambos, T. A.; Schaaf, C.; Schott, J. R.; Sheng, Y.; Storey, J.; Vermote, E.; Vogelmann, J.; White, J. C.; Wynne, R. H.; and Zhu, Z. ~~et al.~~: Current status of Landsat program, science, and applications, *Remote Sensing of Environment* 225, pp. 127–147, doi: 10.1016/j.rse.2019.02.015, 2019.

Wulder, M. A.; Roy, D. P.; Radeloff, V. C.; Loveland, T. R.; Anderson, M. C.; Johnson, D. M.; Healey, S.; Zuh, Z.; Scambos, C. J.; Masek, J. G.; Hermosilla, T.; White, J. C.; Belward, A. S.; Schaaf, C.; Woodcock, C.; Huntington, J. L.;

Lymburner, L.; Hostert, P.; Gao, F.; Lyapustin, A.; Pekel, J. F.; Strobel, P.; and Cook, B. D. et al.: Fifty years of Landsat science and impacts, *Remote Sensing of Environment* 280, p. 113195, doi: 10.1016/j.rse.2022.113195, 2022.

Zemp, M.; Hoelzle, M.; and Haeberli, W.: Distributed modelling of the regional climatic equilibrium line altitude of glaciers in the European Alps, *Global and Planetary Change* 56 (1-2), pp. 83–100, doi: 10.1016/j.gloplacha.2006.07.002, 2007.

Zhang, Z.; Xu, J. l.; Liu, S. Y.; Guo, W. Q.; Wei, J. F.; and Feng, T.: Glacier changes since the early 1960s, eastern Pamir, China, *J. Mt. Sci.* 13 (2), pp. 276–291, doi: 10.1007/s11629-014-3172-4, 2016.